



MACv2-SP: a parameterization of anthropogenic aerosol optical properties and an associated Twomey effect for use in CMIP6

Bjorn Stevens¹, Stephanie Fiedler¹, Stefan Kinne¹, Karsten Peters¹, Sebastian Rast¹, Jobst Müsse¹, Steven J. Smith², and Thorsten Mauritsen¹

¹Max Planck Institute for Meteorology, Hamburg, Germany

²Joint Global Change Research Institute, Pacific Northwest National Laboratory, College Park, MD, USA

Correspondence to: Bjorn Stevens (bjorn.stevens@mpimet.mpg.de)

Received: 15 July 2016 – Published in Geosci. Model Dev. Discuss.: 1 August 2016

Revised: 18 November 2016 – Accepted: 7 December 2016 – Published: 1 February 2017

Abstract. A simple plume implementation of the second version (v2) of the Max Planck Institute Aerosol Climatology, MACv2-SP, is described. MACv2-SP provides a prescription of anthropogenic aerosol optical properties and an associated Twomey effect. It was created to provide a harmonized description of post-1850 anthropogenic aerosol radiative forcing for climate modeling studies. MACv2-SP has been designed to be easy to implement, change and use, and thereby enable studies exploring the climatic effects of different patterns of aerosol radiative forcing, including a Twomey effect. MACv2-SP is formulated in terms of nine spatial plumes associated with different major anthropogenic source regions. The shape of the plumes is fit to the Max Planck Institute Aerosol Climatology, version 2, whose present-day (2005) distribution is anchored by surface-based observations. Two types of plumes are considered: one predominantly associated with biomass burning, the other with industrial emissions. These differ in the prescription of their annual cycle and in their optical properties, thereby implicitly accounting for different contributions of absorbing aerosol to the different plumes. A Twomey effect for each plume is prescribed as a change in the host model's background cloud-droplet population density using relationships derived from satellite data. Year-to-year variations in the amplitude of the plumes over the historical period (1850–2016) are derived by scaling the plumes with associated national emission sources of SO₂ and NH₃. Experiments using MACv2-SP are performed with the Max Planck Institute Earth System Model. The globally and annually averaged instantaneous and effective aerosol radiative forcings are estimated to be -0.6 and -0.5 W m⁻², respectively. Forcing from aerosol–cloud interactions (the

Twomey effect) offsets the reduction of clear-sky forcing by clouds, so that the net effect of clouds on the aerosol forcing is small; hence, the clear-sky forcing, which is more readily measurable, provides a good estimate of the total aerosol forcing.

1 Introduction

Attempts to understand how the anthropogenic aerosol affects the climate system have tended to focus on the quantification of its radiative forcing. One way to do this is to characterize the physical properties of the aerosol given knowledge of aerosol and aerosol precursor emissions. Given the aerosol physical properties, optical and cloud active properties can be inferred and used to quantify aerosol radiative forcing. This bottom-up approach has proven to be challenging. One reason is that important aerosol processes remain poorly understood (Boucher et al., 2013; Carslaw et al., 2013). Another reason is the enormous scale divide between the processes that are understood and those that can be represented with fidelity in a large-scale model. Even processes that are well understood prove difficult to implement consistently (e.g., Stevens and Feingold, 2009). From this perspective, it is not surprising that independent efforts adopting bottom-up approaches yield estimates of aerosol radiative forcing that differ widely (Shindell et al., 2013; Myhre et al., 2013; Boucher et al., 2013).

Rather than asking how our understanding of aerosol processes constrains aerosol radiative forcing, a top-down approach asks how the response to a given distribution of

aerosol optical and cloud active properties is consistent with the observational record. Present bounds on aerosol radiative forcing are largely a result of such approaches (Murphy et al., 2009; Stevens, 2015). The goal of the paper is to describe a simple and easy-to-implement aerosol climatology that we have developed to help advance the top-down approach for constraining aerosol radiative forcing.

The idea of using the response of the climate system to a hypothetical (aerosol) forcing as a test of that forcing is at the heart of detection and attribution studies, and presupposes some understanding of the pattern of aerosol forcing and the pattern of the response. For instance, it has been argued that a strong aerosol forcing, which would have been disproportionately concentrated around the source regions in the Northern Hemisphere, is inconsistent with the strong pattern of Northern Hemisphere warming through the first part of the last century (Stevens, 2015). But this argument assumes that warming in the Northern Hemisphere, especially in the Atlantic sector, could not have been as large as the warming observed if the net radiative forcing over the hemisphere, or region, was negative. This need not be the case, as enthalpy may have been imported into the region at a rate that more than offsets the local negative forcing. To test the idea, it would be helpful to see if robust climate responses can be attributed to patterns of aerosol forcing, for which the ability to prescribe the same pattern of forcing across many climate models is a prerequisite.

Given that the 20th century witnessed a large human imprint on the atmospheric aerosol, it seems natural to ask what was different about the climate of the 20th century due to this anthropogenic aerosol. Published studies, usually based on the response of an individual model, hint that aerosol perturbations may be responsible for shifts in patterns of monsoon rainfall (Bollasina et al., 2011), decadal variability in the Atlantic which may have led to a suppression of hurricane activity (Khain et al., 2010), diminished sunlight at the surface over Europe (Wild, 2012) and the conspicuous decrease in temperature over the eastern and central United States during the middle of the last century (Leibensperger et al., 2012). But these ideas have proven controversial: the response of the intertropical convergence zone (ITCZ) is sensitive to the representation of the cloud processes (Voigt et al., 2014); a purportedly strong North Atlantic cooling by the aerosol appears to be inconsistent with the subsurface temperature record (Zhang et al., 2013), and variations in the surface energy budget are difficult to extract from the noise of natural variability, particularly at high latitudes (Deser et al., 2014). Coincident shifts in large-scale modes of natural variability confound attempts to link climate responses to aerosol forcing. For example, the Pacific Decadal Oscillation changed sign in the 1970s, at the same time that aerosol forcing is thought to have maximized over the Atlantic sector (Meehl et al., 2009). Clearly, a deeper understanding of how the climate system responds to regional heating anomalies would provide a stronger foundation for quantifying the role of

aerosol forcing. Toward this end, a simple method for prescribing aerosol-like anomalies in atmospheric composition would be useful.

These thoughts motivated us to develop a simple parameterization of anthropogenic aerosol optical properties and the effect of the anthropogenic aerosol on the radiative properties of clouds for use in climate models. We aimed to develop an analytic description of the anthropogenic aerosol capable of representing its observed spatiotemporal and spectral variability. Similar, albeit even more simplistic, approaches have been attempted in the past (Tanré et al., 1984), but not for the purpose of studying aerosol changes, and without the benefit of modern observations. Our chosen description would be fit to the present-day observational record, and scaled backward and forward in time to capture past or future changes in aerosol and aerosol precursor emissions. An analytic, albeit empirical, description was desirable to avoid regriding a base climatology for a particular model resolution, and to reduce the input data volume, particularly given the importance and emphasis on the use of higher-resolution simulations in the future. An ability to vary the aerosol properties over time is necessary to represent scenarios of past and possible future effects of anthropogenic activity. In contrast to comprehensive aerosol–chemistry–climate models, we sought an approach that would be computationally lightweight, easy to implement and modify, yet similarly compelling in its ability to represent aerosol radiative forcing. By describing the aerosol in terms of its optical properties and its effect on cloud-droplet population densities, we reduce the chance of introducing discrepancies in forcing that may arise from different choices for how to couple parameterizations of aerosol physical properties to parameterizations of clouds and radiation. It is our hope that the methods we develop will provide a welcome complement to comprehensive aerosol models, spur research into how the climate system responds to forcing and help clarify what degree of detail in the representation of aerosol radiative forcing can lead to a response that is measurable against the noisy background of natural variability.

The organization of the paper is as follows. In Sect. 2, we describe the aerosol distribution component of the parameterization, which is fit to an observational climatology developed for the year 2005. In Sect. 3, we propose an approach for linking anthropogenic aerosol optical depth to changes in cloud active properties. Our representation of the 2005 aerosol distribution and aerosol radiative effects, including induced changes on the scattering cross section and albedo of clouds, is evaluated in Sect. 4 using global simulations with the Max Planck Institute Earth System Model, the MPI-ESM. In Sect. 5, we describe a procedure for scaling the 2005 climatology over the historical period using anthropogenic aerosol and aerosol-precursor emission estimates from different geographic regions, and show how a similar approach can be adopted to projected future emissions. The approach and our main results are summarized in Sect. 6.

Table 1. Names, location and characteristics of individual plumes. Plumes which have a non-harmonic contribution to their annual cycle have larger amplitude (90–100 %) annual variations.

No.	Source region	Lat.	Long.	Type	Main features of annual cycle
1	Europe	49.4	20.6	Industrial	Amplitude 25 %, May max
2	North America	40.1	277.5	Industrial	Amplitude 30 %, July max
3	East Asia	30.0	114.0	Industrial	Amplitude 15 %, biharmonic, Oct and Apr max
4	South Asia	23.3	88.0	Industrial	Amplitude 10 %, maximum in mid-July
5	North Africa	3.5	22.5	Biomass	Non-harmonic, Dec max, Mar–Oct min
6	South America	−10.3	298.0	Biomass	Non-harmonic, Sep max, Jan–Jun min
7	Maritime Continent	−1.0	106.0	Biomass	Non-harmonic, Sep max, Jan–Jun min
8	South central Africa	−3.5	16.0	Biomass	Non-harmonic, Aug max, Jan–Dec min
9	Australia	−20.0	135.0	Industrial	Amplitude 60 %, Sep max

2 Simple plumes as basis functions for representing anthropogenic aerosols

Our basic idea is to associate spatial plumes of anthropogenic aerosols with emissions from source regions. The plumes are constructed by fitting to a climatology for the present-day (2005) distribution of anthropogenic aerosol optical depths in the mid-visible (550 nm) range. To capture past changes, the amplitude of these plumes will be scaled with the strength of the anthropogenic emissions within the source region. Major anthropogenic emissions are spatially compact, at least from a planetary perspective. This motivates the adoption of a small number of plumes as basis functions for representing anthropogenic aerosol optical properties and cloud active properties. For simplicity, we consider two plume types: one that is dominated by emissions from industrial emissions, the other from biomass burning. Hereafter, we refer to these as industrial and biomass plumes, respectively, even though each plume really composites over a mixture of source activities. The industrial and biomass plumes are distinguished by the strength of their seasonal cycle, their single-scattering albedo, and their cloud-droplet population density susceptibility to anthropogenic aerosol perturbations.

The plumes are designed to fit the 2005 distribution of mid-visible anthropogenic aerosol optical depth as described by the Max Planck Institute Aerosol Climatology, MAC (Kinne et al., 2013). MAC provides estimates of monthly mean aerosol optical properties at a spatial resolution of 1° of latitude by 1° of longitude. Climatological values of aerosol properties are derived from high-quality data by ground-based sun-photometer networks (AERONET; Holben et al., 2001) merged onto background maps from global models participating in the Aerosol Model Intercomparison Project (AeroCom). The merging is performed for different aerosol properties: aerosol optical depth (AOD) at 440, 550 and 870 nm, absorbing AOD at 550 nm and, in addition, for contributions to these properties by coarse-mode particles or fine-mode aerosol particles. The merged fine-mode AOD (at 550 nm), along with a scaling factor (anthropogenic fraction) based on fine-mode AOD output of com-

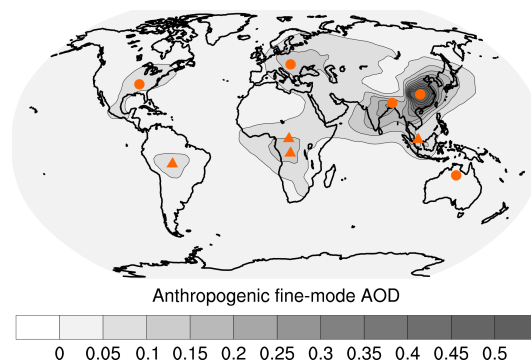


Figure 1. Global distribution of annually averaged anthropogenic aerosol optical depth τ_a at 550 nm. Also indicated are the locations of MACv2-SP plume centers. Industrial and biomass plumes are distinguished by the choice of symbol: circles for industrial plumes and triangles for biomass plumes.

prehensive aerosol–chemistry models, run for present-day and pre-industrial conditions, define the anthropogenic AOD (at 550 nm) map of MAC. An anthropogenic contribution to the coarse mode is assumed negligible. MACv2 (MAC version 2), provides the baseline that the plume concept of MACv2-SP attempts to approximate. MACv2 was adopted because it incorporates a number of improvements compared to version 1, specifically (i) oceanic reference data (from the Maritime Aerosol Network – MAN; Smirnov et al., 2009) are now included; (ii) aerosol extensive optical properties are merged; and (iii) on average, a roughly 30 % lower anthropogenic fine-mode AOD fraction is assumed, yielding an anthropogenic AOD more in line with other estimates. Adopting simple plumes as basis functions to represent the anthropogenic aerosol could be adapted to any climatology, but to reflect its origins in MACv2, hereafter we refer to our model as MACv2-SP.

Nine plumes (five industrial and four biomass) appear to adequately capture the spatial distribution of the anthropogenic aerosol of MACv2. The names given to the individual plumes, the location of the plume centers and the type of

each plume is summarized in Table 1 and illustrated in Fig. 1 relative to the 2005 annual mean of MACv2. The plume centers are placed where the local AOD, as represented by MACv2, maximizes. Even for a perfect climatology this need not coincide with the location where emissions maximize, as the AOD is influenced by deposition and transport. The use of two plumes (north and south central Africa) in close proximity, to define the contribution to anthropogenic AOD over Africa, enables a better representation of different seasonal cycles.

A basic premise in the development of MACv2-SP is that the shape of individual plumes is independent of the strength of the source. This assumption is reasonable as long as effects from changes in the atmospheric circulation remain small relative to uncertainty in the aerosol pattern for a given source. The lack of a clear signal of a feedback on the aerosol forcing from changes in the climate supports this assumption (Boucher et al., 2013). A climatological approach omits, however, the coupling between synoptic systems and the aerosol. This may be important to the aerosol effect: experience suggests that rainier days are cloudier, but also less aerosol laden at near-surface levels. Hence, prescribing the time mean aerosol may result in a larger radiative forcing than would arise from an aerosol with the same time mean properties, but which was allowed to interact with the circulation, i.e., the bistability hypothesis of Baker and Charlson (1990). These effects, which are expected to be more pronounced for aerosol–cloud interactions, are accounted for in MACv2-SP by setting the spatial and seasonal pattern of the aerosol based on MACv2, but allowing a degree of freedom in the specification of its amplitude. In MACv2-SP, the eventual amplitude of the forcing, though guided empirically, is in effect a test quantity. The idea to use the flexibility of the parameterization to see what amplitude of forcing produces a response that is difficult to reconcile with the instrumental record (of, say, temperature). Studies using a similar approach (e.g., Stevens, 2015; Pincus et al., 2016) have suggested that this may help provide better bounds on the magnitude of aerosol radiative forcing.

Mathematically, MACv2-SP provides a five-dimensional (three spatial dimensions, time and wavelength) description of the anthropogenic aerosol optical properties. The climatology is built around a description of the volume extinction, e_a , at 550 nm. In a second step, described later, the wavelength dependence of the extinction is accounted for, and additional optical properties are specified. Unless an explicit wavelength dependence is specified, all properties are assumed valid at 550 nm.

The total volume extinction of mid-visible radiance by the anthropogenic aerosol, e_a , is given as the emission-weighted sum of the extinction from nine different plumes:

$$e_a(x, y, z, t) = \sum_{i=1}^9 e_i(x, y, z, t_f(t)) E_i(t_y(t)). \quad (1)$$

Here, e_i defines the extinction associated with the i th plume for the year 2005, and E_i the emissions scaling. Year-to-year variations are separated from annual variations by describing the time dependence by two separated time variables. The emission scaling depends on $t_y(t)$, which denotes an integer year number,

$$t_y(t) := \lfloor t/1 \rfloor, \quad (2)$$

which can be, for example, 1966 or 2008. The annual cycle depends on the year fraction, $t_f(t) = t - t_y$. In principle, t_f is a real number defined over the unit interval; in our present implementation, the annual cycle changes discretely over 52 intervals, i.e., roughly on a weekly basis.

The optical path over a layer is defined as the integral of the volume extinction,

$$\tau(x, y, t) = \int_{z_1}^{z_2} e(x, y, z, t) dz \quad (3)$$

In the event that the path is over the entire atmospheric column, it is referred to as the optical depth. Unless explicitly specified, it is assumed that the interval corresponds to the entire depth of the atmosphere, in which case we speak of the column integral or the anthropogenic aerosol column optical depth.

2.1 Plume spatial structure

The spatial structure of the e_i values are given through the superposition of two individual features (or sub-plumes) weighted by an annual cycle. For these features, we have chosen rotated quasi-Gaussian functions, such that

$$e_i(x, y, z, t_f) = \tau_i b_i(x, y, z) \times \sum_{j=1}^2 a_{ij}(t_f) \exp\left(-\frac{1}{2} \langle \mathbf{x}_i, \mathbf{R}_{ij} \mathbf{A}_{ij}^{-1} \mathbf{R}_{ij}^{-1} \mathbf{x}_i \rangle\right), \quad (4)$$

$$\mathbf{x}_i = \begin{pmatrix} x - x_i \\ y - y_i \end{pmatrix}. \quad (5)$$

Here, i denotes the plume number, j the feature number, $a_{ij}(t_f)$ is the feature weighting in an annual cycle, $b_i(x, y, z)$ the vertical weighting, τ_i the column optical depth of the i th plume at its center in the reference year (2005) and (x_i, y_i) the latitude and longitude of the plume centers. The feature weights a_{ij} are split into time weights $w_{ij}(t_f)$, describing the annual cycle, and relative feature weights f_{ij} , giving a specific weight to each feature. Hence, $a_{ij}(t_f) = f_{ij} w_{ij}(t_f)$, and is constructed to guarantee that $\sum_j \int_0^1 a_{ij}(t_f) dt_f = 1$. The feature weights are plume dependent and are chosen so that the spatial pattern of MACv2 is reproduced by MACv2-SP, and τ of MACv2 and MACv2-SP are the same at the plume center.

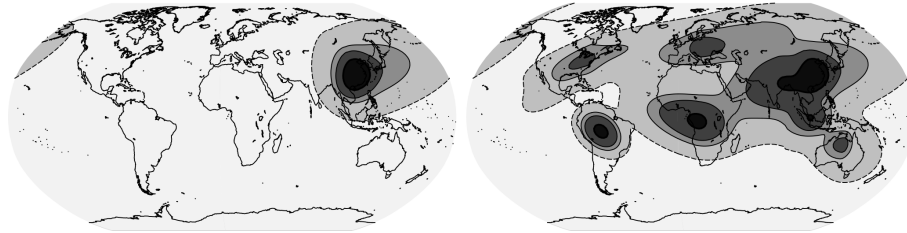


Figure 2. Horizontal spatial pattern of the anthropogenic aerosol optical depth plumes. Single east Asian plume is on the left; all nine plumes, right. Contour levels are 0.005 (dashed), 0.05, 0.1 and 0.3 (thickened). Plumes are shown for September 2005, a time of year when there is also a substantial anthropogenic contribution from tropical and Southern Hemisphere biomass burning.

2.1.1 Horizontal structure

To better represent the near- and far-field aerosol distributions, as seen in MACv2, two features are adopted for each plume, as shown in Eq. (5). One is shaped like a Gaussian feature; the other is only piecewise Gaussian. The Gaussian feature is chosen to be rotationally symmetric and is introduced to represent the near-field AOD structure in the vicinity of the source. The quasi-Gaussian features are elongated to mimic asymmetric transport with prevailing winds and a possibly asymmetric distributions of sources and sinks. The covariance matrix \mathbf{A}_{ij} describes the latitudinal and longitudinal extent of each piecewise Gaussian feature such that

$$\mathbf{A}_{ij} = \begin{cases} \begin{pmatrix} \sigma_{W,ij}^2 & 0 \\ 0 & \sigma_{W,ij}^2 \end{pmatrix}, & \text{if } (x - x_i) \leq 0 \\ \begin{pmatrix} \sigma_{E,ij}^2 & 0 \\ 0 & \sigma_{E,ij}^2 \end{pmatrix}, & \text{if } (x - x_i) > 0. \end{cases} \quad (6)$$

The components of \mathbf{A}_{ij} are chosen subjectively so as to reasonably fit the climatology.

The horizontal orientation of the plumes is also controlled by the rotation matrix \mathbf{R}_{ij} :

$$\mathbf{R}_{ij} = \begin{pmatrix} \cos(\theta_{ij}) & -\sin(\theta_{ij}) \\ \sin(\theta_{ij}) & \cos(\theta_{ij}) \end{pmatrix}. \quad (7)$$

The angles θ_{ij} are tuned for each plume and feature to match the MACv2 monthly climatology. For instance, the midlatitude plumes point northeastward from the centers, which can be attributed to prevailing westerlies and, in the case of North America, the distribution of sources.

Adopting simple plumes as basis functions for representing the aerosol reasonably captures the spatial patterns of the observed plumes. This is illustrated in Fig. 2, whose left panel first shows the structure of a single (east Asian) plume for the month of September 2005. Here, many features of the plume construction are evident, e.g., the asymmetry and the rotation of its major axis relative to the cardinal directions. The composite structure that emerges when all nine plumes are activated is also shown in Fig. 2 (right). Here, eight plume

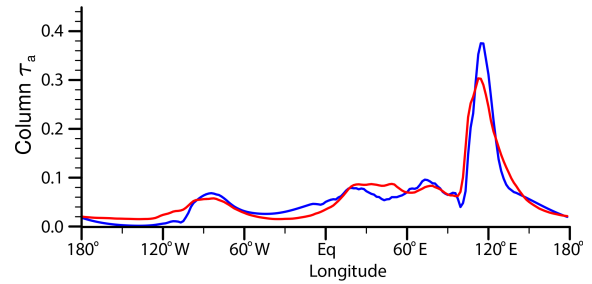


Figure 3. Annual (2005) mean anthropogenic aerosol optical depth (550 nm) between 30 and 60° N for MACv2-SP (blue) and MACv2 (red).

centers can be identified, with the east Asian, Indian and Indonesian biomass plume forming a tri-polar structure. The north central African plume is weak during boreal summer and subsumed in the south central African plume so that it is not evident as a distinct feature.

Figure 3 compares τ , averaged over the latitudes from 30 to 60° N. Even with a relatively small number of degrees of freedom, MACv2-SP can capture many of the details of the spatial structure as represented in the original MACv2 climatology.

2.1.2 Vertical structure

The aerosol optical depth is distributed over height by b_i , chosen as the kernel of Euler's β function ($B(p, q) = \int_0^1 \eta^{p-1} (1 - \eta)^{q-1} d\eta$). The Heaviside function, \mathcal{H} , is introduced to ensure that the plume is only defined above the surface and below a specified height, z_{\max} . Thus,

$$b_i(x, y, z; p_i, q_i) = \left(\frac{\eta^{p_i-1} (1 - \eta)^{q_i-1}}{B(p_i, q_i)} \right) \mathcal{H}(z - z_g(x, y)),$$

with $\eta = \begin{cases} z/z_{\max} & \text{if } z \leq z_{\max} \\ 0 & \text{otherwise} \end{cases} \quad (8)$

The parameters p_i and q_i define the kernel of the β function for the i th plume and are tuned to reproduce the vertical distribution of the fine-mode MACv2 AOD averaged over a 20° longitude by 20° latitude box about the plume center.

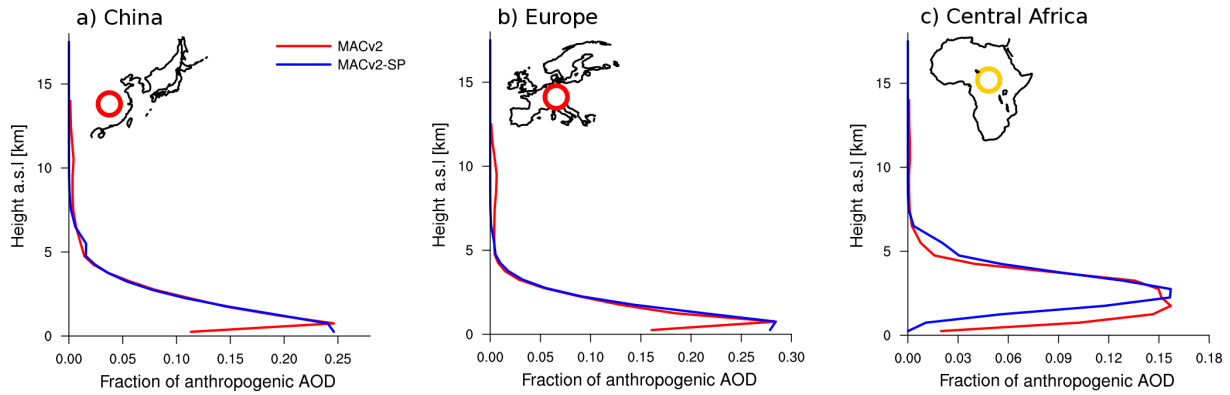


Figure 4. Vertical profile of fractional aerosol optical depth (550 nm) from MACv2-SP with respect to the column integral at each location (x, y). Shown by the blue lines are b_i values (i.e., the fraction of the AOD) for the east Asian, European and central African plume; red is the distribution taken from MACv2.

The height, z_{\max} , is specified to be 15 km to ensure that the plume does not extend into the middle and upper atmosphere, where its shape would no longer be dominantly constrained by the processes in the troposphere. Normalization by the β function, $B(p_i, q_i)$, ensures that the vertical weighting does not change the column optical depth, except in the case when $z(x, y)$ extends below the surface. In the implementation, the discrete integral of the β function is formed to ensure that this relation is also satisfied discretely. Prescribing the vertical distribution in this manner, whereby the vertical weighting is first defined from the distance above the sea surface, ensures that plumes whose origins are in low-lying areas (which is the case for each of our plumes) do not unrealistically extend over neighboring topography, as they would otherwise. The improvement this introduces over regions of topography is evident, for instance, over southeast Asia, as shown in Fig. 2. It implies that the aerosol optical depth is reduced over elevated terrain. If the climatology were to be extended to include elevated source regions, this prescription should be modified.

Figure 4 shows b_i for three plumes compared to the fractions from MACv2.0. The largest extinction occurs in low levels for all plumes. Maxima in the tropics, e.g., central Africa, shown in Fig. 4c, are shifted to higher altitudes compared to the extratropics, e.g., China and Europe (Fig. 4a–b), consistent with deeper mixing over Africa, particularly in the dry season.

2.2 Annual cycle

Individual plumes can have their own annual cycle, whose relative amplitude is assumed to be independent of year-to-year variations in emissions. This is what one expects if the annual cycle is determined mostly by meteorology, for instance, as in the case of open burning where meteorology influences both the aerosol sinks (wet deposition) and sources (availability and condition of fuel). The annual cycle is fit to

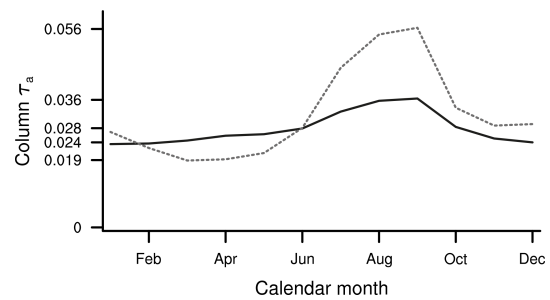


Figure 5. Variation of the column and globally averaged anthropogenic aerosol optical depth (550 nm) over the annual cycle. Shown are values for the year 2005 for the global average (solid) and for the deep tropics equatorward of 15° (dashed).

MACv2, and is particularly pronounced over biomass burning regions.

For all but two plumes, the same time weights w_{ij} are applied to both of its features. The exceptions are the South American and south African plumes, which have different annual cycles for each feature. The annual mean value of the time weights is specified to be unity, i.e., $\int_0^1 w_{ij}(t_f) dt_f = 1$. Currently, we define two types of annual cycles. The first type is a small one for industrial plumes, which is given as a harmonic perturbation about the annual mean,

$$w_{ij}(t_f) = 1 - c_{ij} \cos(n\pi(t_f - \phi_{ij})), \quad (9)$$

with c_{ij} the annual component, ϕ_{ij} the phase and n an integer. For all but the east Asian plume, $n = 2$, defining a single annual cycle. For east Asia, $n = 4$, thereby leading to a semi-annual cycle, e.g., Table 1. The second type of annual cycle is given by linearly interpolating to specified monthly values to fit the non-harmonic annual cycle of biomass burning plumes that emerges in MACv2.

Figure 5 shows the monthly mean of the globally averaged τ_a and the mean just for latitudes equatorward of 15° to illus-

Table 2. Optical properties as a function of plume type. Here, ω_i denotes the mid-visible (550 nm) single-scattering albedo, γ_i the asymmetry parameter (also at 550 nm) and α the Ångström coefficient in Eq. (10).

Plume type	$\omega_{i,550}$	$\gamma_{i,550}$	α
Industrial	0.93	0.63	2.0
Biomass	0.87	0.63	2.0

trate the effect of the seasonal scaling. The global annual cycle is mostly carried by the biomass burning plumes in the deep tropics. These biomass plumes are most pronounced in the boreal summer or the dry season over tropical land masses in the Southern Hemisphere. It remains debatable as to whether the annual cycle in aerosol forcing projects detectably onto the climate system, something that MACv2-SP can be easily used to test.

2.3 Wavelength-dependent optical properties

The spectral (wavelength) dependance of the anthropogenic aerosol extinction is specified through an Ångström parameter, α_i , such that

$$e_i(x, y, z, t, \lambda) = e_i(x, y, z, t) \exp \left[-\alpha_i \ln \left(\frac{\lambda[\text{nm}]}{550 \text{ nm}} \right) \right]. \quad (10)$$

The index i indicates the Ångström parameter may vary from plume to plume. The aerosol optical path is geometrically related to the extinction by Eq. (3), but in the two-stream approximation its effect on radiative transfer also requires spectral-dependent information for the asymmetry factor and single-scattering albedo of the aerosol.

The anthropogenic aerosol is assumed to be small in size (ca. 150 nm in radius), so that the Ångström parameter is near 2.0, and prescribed to adopt this value. For the single-scattering albedo, properties averaged over 20° latitude by 20° longitude regions around plume centers suggest that $\omega_i = 0.93$ for urban pollution and $\omega_i = 0.87$ for plumes dominated by seasonal biomass burning, as summarized in Table 2. To extend these values to other wavelengths, we assume they are constant over the ultraviolet and visible regions of the solar spectrum (200–700 nm) but are reduced in the near-infrared (from 700–3000 nm). This reduction arises from the small aerosol size, which in the Rayleigh limit of the wavelength becoming much larger than the particle requires a reduction to both single-scattering albedo and the asymmetry factor.

For the single-scattering albedo $\omega_i(\lambda)$ of the plume i , we adopt

$$\omega_i(\lambda) = \omega_i \cdot \begin{cases} [\omega_i + (1 - \omega_i) \Lambda^3]^{-1} & \text{for } \Lambda > 1 \\ 1 & \text{otherwise,} \end{cases} \quad (11)$$

where

$$\Lambda := \frac{\lambda[\text{nm}]}{700 \text{ nm}}. \quad (12)$$

The Λ^3 dependance in this expression is motivated by the fact that in the Rayleigh limit, absorption is inversely proportional to the wavelength and scattering scales with λ^{-4} , so that their ratio is proportional to λ^3 .

The asymmetry parameter $\gamma_i(\lambda)$ is likewise adjusted for wavelengths larger than 700 nm such that

$$\gamma_i(\lambda) = \gamma_i \cdot \begin{cases} \Lambda^{-1/2} & \text{for } \Lambda > 1 \\ 1 & \text{otherwise.} \end{cases} \quad (13)$$

In all cases, the effect of the aerosol on the transfer of radiant energy at wavelengths larger than 3000 nm (which, in a practical sense, applies to the treatment of longwave radiative transfer solvers) is neglected, consistent with the assumption that the anthropogenic aerosol predominates in the fine mode. The final spatial optical properties arising from the superposition of different plumes are calculated by optical depth weighting (or, in the case of the asymmetry factor, by the optical-depth-weighted single-scattering albedo) as is customary.

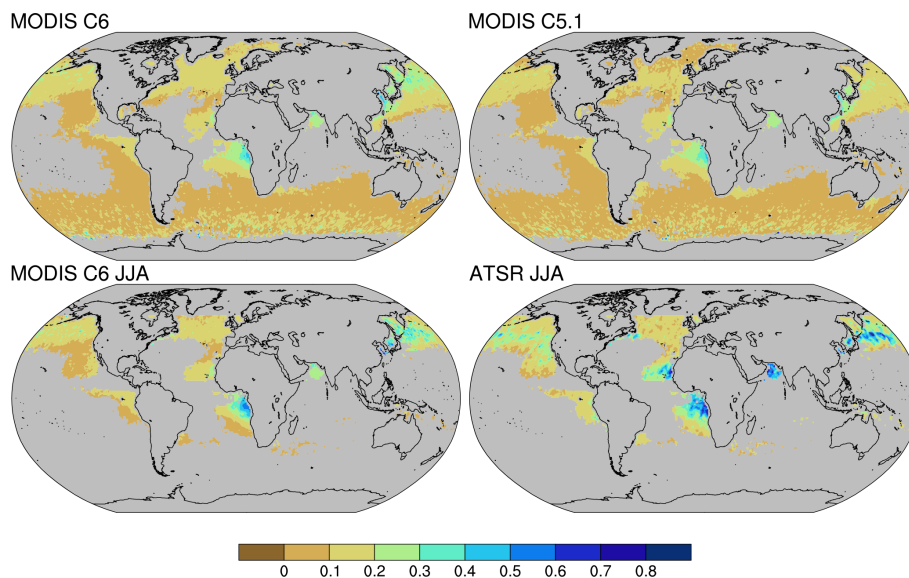
The values of the plume aerosol properties are based on AERONET data, and as such are consistent with an earlier analysis of that data by Dubovik et al. (2002). However, the use of constant values to capture the average property of a plume considerably belies local variability. To what extent such details are important for the climate response to aerosol forcing is unknown, but MACv2-SP makes it possible to explore this question.

3 Cloud active properties

To derive a relationship between the anthropogenic aerosol and cloud properties, we first explored the relationship between the fine-mode aerosol optical depth, τ_f , and cloud-droplet population densities, N . The spatial association between estimates of the two quantities is available from satellite observations and from modeling. Three different satellite datasets, described at a spatial (latitude, longitude) resolution of 1°, are considered. Two datasets are from different processing versions of the MODIS (Moderate Resolution Imaging Spectroradiometer) sensor data, and one is based on the AATSR (Advanced Along Track Scanning Radiometer) sensor data. MODIS, due to its wider swath, offers more samples than AATSR does. A minimum τ_f of 0.05 was adopted to ensure retrieval reliability. Further details of these data are summarized in Table 3. Similarly, monthly averaged output from different global aerosol models participating in the AeroCom project (Schulz et al., 2006; Kinne et al., 2006) was also analyzed. The N values were derived for levels warmer than the melting level from the indirect effect analysis of Quaas et al. (2009), and monthly averages of τ_f were

Table 3. Satellite data used to evaluate the relationship between fine-mode optical depth and cloud-droplet population density.

Platform	Description
MODIS collection 5.1	Level 3 data are from NASA's EOS-Aqua platform for the 12 months from December 2006 to November 2007. Retrievals of cloud-droplet population densities, N , assume that they are constant throughout the cloud and that the liquid water is linearly increasing with height in the cloud. Estimates of N are derived using the multispectral method (Nakajima et al., 1991) by combining simultaneous retrievals of both cloud optical depth and droplet radius at the cloud top. See Grosvenor and Wood (2014) for further details. Corresponding τ_f data are taken from NASA's LAADS website.
MODIS collection 6.0	Level 3 data are from NASA's EOS-Aqua platform for the 12 months from January to December 2008. Estimates of the cloud-droplet population density are based on the assumption of adiabatic stratification (Bennartz, 2007; Brenguier et al., 2000) and were provided by John Rausch of Vanderbilt University. Corresponding τ_f data were pulled from NASA's LAADS website.
AATSR	Data are from ESA's ENVISAT platform for the 3-month period (Jun–Aug 2008). CDNC and τ_f data were retrieved with the Oxford-RAL aerosol and cloud (ORAC) retrieval algorithm (Thomas et al., 2011) and data for CDNC and τ_f were provided by Matthew Christensen from the Rutherford Appleton Laboratory.

**Figure 6.** Fine-mode aerosol optical depth (at 550 nm) from different satellite retrievals. Shown are annual averages of MODIS collection 6 for 2008 (upper left), MODIS collection 5.1 for 2007 (upper right); boreal summer (JJA) 2008 averages of MODIS collection 6 (lower left) and boreal summer (JJA) for AATSR-ORAC (lower right). Grey indicates no data.

analyzed for both the pre-industrial (1850) and present-day (2005) conditions (Myhre et al., 2013). Model output was re-gridded to the spatial resolution (1° in latitude by 1° in longitude) of the satellite data for subsequent analysis.

The relationships between τ_f and N in global modeling are quite diverse and, on average, stronger than suggested by observations. In contrast, the satellite retrievals are more consistent, even though spatial (and temporal) coverage is limited to overcast oceanic regions. For this reason, our parameterization is founded on the satellite data; nonetheless, the relationship we derive remains consistent with the modeling given the large model spread.

Values of fine-mode optical depth and cloud-droplet population densities, $\{\tau_f, N\}$, retrieved from satellite measure-

ments are presented in Figs. 6 and 7. The MODIS collection 6 data are presented for the annual average and for the boreal summer season to allow for comparison with MODIS collection 5.1 (annual) and AATSR (seasonal). Due to quality control requirements, whereby retrievals are avoided in broken cloud scenes, the displayed data locations represent only a subset of the actually available data for τ_f and N .

Overall, the retrievals suggest that there is a relationship between τ_f and N . For instance, regions of elevated τ_f over the eastern-boundary currents in the Atlantic, near the Indian subcontinent, west of Japan and between Japan and the Asian mainland (Fig. 6) also correspond to elevated values of N (Fig. 7). The presence of an apparent relationship is consistent with previous work. Andreae (2009), for instance,

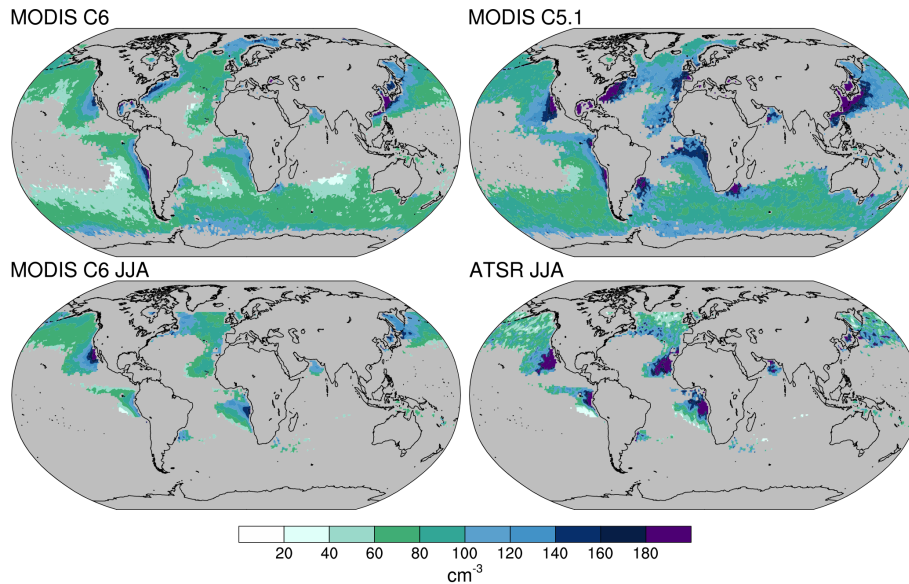


Figure 7. Annually averaged N from different satellite retrievals. Shown are MODIS collection 6 for 2008 (upper left) and MODIS collection 5.1 for 2007 (upper right); boreal summer (JJA) 2008 averages of MODIS collection 6 (lower left) and boreal summer (JJA) for AATSR-ORAC (lower right). Grey indicates no data.

related local observations of total AOD to measurements of cloud condensation nuclei (CCN) and then, in a second step, related values of CCN to N . Some early studies of aerosol radiative forcing also adopted a similar approach (e.g., Boucher and Lohmann, 1995). The correspondence between τ_f and N is not perfect. For example, elevated values of N over the Californian stratocumulus regions (Fig. 6) do not show a commensurately pronounced retrieval of τ_f (Fig. 7) – although even here variability in the background contribution to fine-mode aerosol may mask relationships. In addition, although the retrievals of τ_f from the different satellite platforms are broadly consistent, estimates of N are much more variable and show systematic differences across the various products. Retrievals of N based on MODIS collection 5.1 yield much larger estimates than those based on collection 6.0 (e.g., Table 3).

The covariation between τ_f and N is quantified through a consideration of all of the available data, as shown in Fig. 8. To construct this figure, retrieved values of N are binned as a function of τ_f drawn from clear-sky retrievals in the same geographic region. Shown are retrievals from satellite data (upper panel) and model output (lower panel). Values of $\tau_f > 0.25$ were excluded due to insufficient samples. The data of the joint histograms are statistically analyzed in 20 τ_f bins. Along the median values in each histogram, logarithmic fits of the form $N \propto \ln(\tau_f)$ have been constructed and are displayed in Fig. 8. Despite considerable scatter, the relationship between N and τ_f is a systematic one: across almost all of the τ_f bins, N increases with τ_f , and this increase becomes smaller for larger τ_f . This is true for both the model output and the retrievals, although the relation-

ship is somewhat stronger in the latter, and a bit less regular. A logarithmic function captures this behavior and is consistent with understanding that an increase in τ_f is expected to be associated with a smaller increase in N the larger N (or τ_f) was to begin with. One reason for such behavior is that with more available cloud condensation nuclei, peak supersaturations reduce, leading to a smaller activated fraction (Twomey, 1959; Ramanathan et al., 2001; Carslaw et al., 2013). Although the exact form of any purported relationship between τ_f and N can be debated, this analysis shows that a logarithmic relationship reasonably represents the data.

This logarithmic relationship forms the basis for representing the Twomey effect in MACv2-SP. The functional form proposed based on the analysis of the satellite data, Fig. 8, gives

$$N = a_N \ln(b_N(\tau_a + \tau_{bg}) + 1), \quad (14)$$

where $\{a_N, b_N, \tau_{bg}\}$ are parameters. For the fit to MODIS C6, $a_N = 16$ and $b_N = 1000$. The value of τ_{bg} scales a spatial pattern of the background fine-mode aerosol that is the same as for τ_a , but is not something that can be derived from the data. It is a tuning parameter. Physically, we associate τ_{bg} with a background contribution to the AOD, as even in a pristine atmosphere cloud condensation nuclei are produced from purely natural processes and assumed to be distributed with the meteorology similar to τ_a . Based on Eq. 14,

$$\frac{N(x, y, t)}{N_{1850}(x, y, t_f)} = \frac{\ln(b_N(\tau_a + \tau_{bg}) + 1)}{\ln(b_N \tau_{bg} + 1)}. \quad (15)$$

By prescribing the MACv2-SP Twomey effect in the form of the ratio N/N_{1850} , it does not interfere with the back-

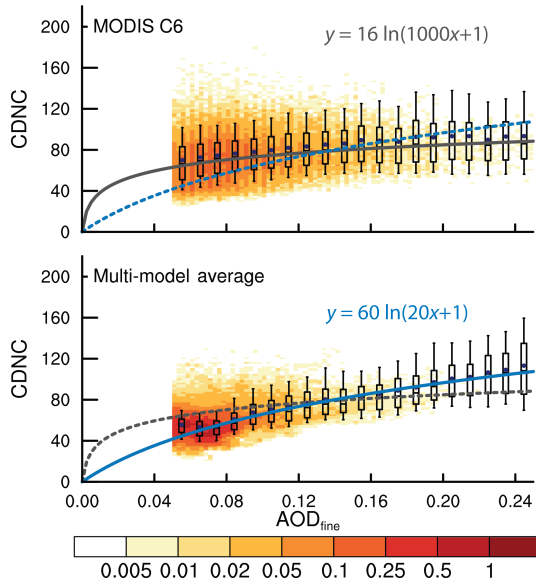


Figure 8. Fine-mode aerosol optical depth and cloud-droplet population density joint histograms based on monthly ($1 \times 1^\circ$) averaged data. Histograms are based on retrievals from MODIS collection 6 (upper) and AeroCom Phase I models. The derived relationship is presented in the upper-right section of each panel based on a fit along the highest frequency of 20 AOD section bins. The data in each AOD bin are summarized by boxes which indicate the 25th and 75th percentiles. The whiskers outside each box indicate the 10th and 90th percentiles; the horizontal line and the dot in each box indicate the median and average, respectively. The solid line denotes the fit to the data in the plot, and the dashed the data in the other plot.

ground (1850) droplet population, N_{1850} , that was used to tune the host model, and it ensures that, all else being equal, the proportional change in N due to the anthropogenic aerosol will be insensitive to N_{1850} . The strength of the Twomey effect in MACv2-SP thus depends largely on the specification of τ_{bg} .

In MACv2-SP, τ_{bg} is calculated identically to τ_a except that there is no emission weighting and the background plume amplitudes (the τ_i in Eq. 5) are chosen to represent the contribution of the pre-1850 aerosol to N_{1850} . These were chosen to be prescribed factors for industrial versus biomass regions with values that gave what are believed to be reasonable, globally and annually averaged droplet concentrations for the present day. A globally uniform background fine-mode AOD of 0.02 is also included on top of the pre-industrial (1850) source contribution so as to represent the effect of distributed sources such as sea salt, or DMS (dimethyl sulfide) emissions, on the background (1850) cloud-droplet population density. Because it describes the background, τ_{bg} is not emission weighted, but adopts values that are fixed in time. In Eq. (15), the possibility of maintaining an annual cycle in the prescription of N_{1850} is indicated by the dependence on t_f , even if in the present implementation of MACv2-

SP such an effect is not implemented. Because τ_{bg} is specified as part of MACv2-SP, it will not necessarily be consistent with the N_{1850} of the models. But given that the purpose is simply to specify a consistent value of N/N_{1850} for all of the models, this is only a formal inconsistency in how one interprets Eq. (15). Its ultimate consequence is that it inhibits models with a cleaner background state from having a larger Twomey effect for the same aerosol perturbation.

Equation (15) is consistent with the data and with understanding, but it is admittedly crude. One could imagine a variety of other relationships fitting the data equally well. Precisely for this reason, we favor a very simple form, as it makes the underlying assumptions transparent and easy to change. Toward this end, in a companion paper, Fiedler et al. (2017) examine in some detail how the effective radiative forcing depends on the form of Eq. (15) and its parameters. Consistent with what was found by Carslaw et al. (2013), it is shown that the strength of the background, τ_{bg} , has the greatest impact on the radiative forcing from aerosol–cloud interactions, and it does so by effectively controlling how far from the plume center aerosol perturbations are allowed to influence cloud properties. If aerosol perturbations are allowed to extend further over the remote oceans, affecting larger regions with a darker surface, a greater (more negative) global mean radiative forcing arises.

4 Time-varying forcing

The year-to-year variations are specified as a time series, $E_i(t_y)$, with t_y denoting the year following a Gregorian calendar. Physically, it can be thought of as the column anthropogenic aerosol optical depth of the i th plume, at the plume center, normalized by its value in a reference year.

$$E_i(t_y) = \tau_i(t_y) / \tau_i(t_{ref}) \quad (16)$$

By definition, $E_i(t_y)$ is unity at $t_y = t_{ref}$. In the present implementation, $t_{ref} = 2005$.

Different approaches to the annual scaling have been considered. One approach is to scale values of τ_i by its ratio in any given year to its ratio in 2005 as calculated by aerosol–climate models. This approach helps account for the variety of processes that likely control AOD and can also be readily extended to the future. This connection to the more comprehensive modeling is attractive, but makes it difficult to change and lacks the transparency we desire. Instead, $E_i(t_y)$ is related to estimates of the past or projections of future emissions. If $\mathcal{E}_{ik}(t_y)$ denotes the annual emissions of component k for plume i , then

$$E_i(t_y) = \frac{\sum_k w_k [\mathcal{E}_{ik}(t_y) - \mathcal{E}_{ik}(1850)]}{\sum_k w_k [\mathcal{E}_{ik}(2005) - \mathcal{E}_{ik}(1850)]}, \quad (17)$$

for $t \geq 1850$,

where w_k denotes the weighting of the k th constituent emission contribution to the plume amplitude, for instance, SO_2 .

Table 4. ISO codes for countries contributing to individual plumes. The union codes of the set of 20 countries with the largest amount of 2014 SO₂ emissions and the set of the 20 countries with the largest total SO₂ emissions since 1850 are indicated in bold.

Plume	ISO code
Europe	alb, aut, bel, bgr, bih, blr, che, cyp, cze, deu, dnk, esp , est, fin, fra , fro, gbr , geo, gib, grc, hrv, hun, irl, isl, isr, ita, jor, lbn, lie, ltu, lux, lva, mda, mkd, mlt, mne, nld, nor, pol , prt, pse, rou, rus , srb, srb (kosovo), svk, svn, swe, tur, ukr
North America	atg, bhs, blz, bmu, can , cub, cym, dma, dom, grl, hti, jam, kna, mex , pri, spm, sxm, tca, usa , vgb, vir
East Asia	chn , hkg, jpn , kgz, kor, mac, mng, twn
South Asia	afg, are, arm, aze, bgd, bhr, btn, ind, irn, irq, kaz , kwt, lka, mdv, mmr, npl, omn, pak , qat, sau , syc, syr, tjk, tkm, uzb, yem
North central Africa	ben, bfa, caf, civ, cmr, cpv, dji, dza, egy, eri, esh, eth, gab, gha, gin, gmb, gnb, gnq, ken, lbr, lby, mar, mli, mrt, ner, nga, sdn, sen, sle, som, ssd, stp, tcd, tgo, tun
South America	abw, arg, bol, bra , brb, chl, col, cri, cuw, ecu, flk, glp, grd, gtm, guf, guy, hnd, lca, msr, mtq, nic, pan, per , prk, pry, slv, sur, tto, ury, vct, ven
Maritime Continent	brn, fsm, gum, idn , khm, lao, mys, phl, plw, png, sgp, slb, tha, vnm
South central Africa	ago, bdi, bwa, cod, cog, com, iso, mdg, moz, mus, mwi, nam, reu, rwa, swz, tza, uga, zaf, zmb , zwe
Australia	asm, aus , cok, fji, kir, mhl, ncl, niu, nzl, pyf, tkl, tls, ton, vut, wlf, wsm

Equation (17) ensures that $E_i(1850) = 0$ and $E_i(2005) = 1$. This prescription has been chosen with application to CMIP6 (Eyring et al., 2016) in mind, as it allows τ_a to be added to the background used by models in their control run, which is traditionally taken as 1850. Hence, the application of the MACv2-SP does not require models to rerun their control simulations. If one is interested in using this method for periods prior to 1850, or for scenarios where $\mathcal{E}_{ik}(t_y) < \mathcal{E}_{ik}(1850)$, the implied negative perturbation may exceed the background, which would require the approach to be revisited. Defining $\mathcal{E}_k(t_y)$ as the global emissions of constituent k , the global weighting, $E(t_y)$, is defined analogously to Eq. (17).

Both SO₂ and NH₃ emissions are allowed to contribute to $E_i(t_y)$. For these emissions, we use estimates from the Community Emissions Data System (CEDS; see <http://www.globalchange.umd.edu/ceds/ceds-cmip6-data/>). The CEDS is a data-driven, open-source framework developed to provide historical emission estimates of aerosol and precursor compounds. These emission data are being released for use as historical forcing input data for CMIP6. So as to capture all emissions, each country in the CEDS is associated with one of our nine plumes, as described by Table 4. The $E_i(t_y)$ are provided as an 11-year averaged value centered on the whole year, e.g., 1910 or 1950. As an example, $E_i(t_{1950})$ is calculated using the emission data from 1945 through 1955 inclusive. Yearly values are then interpolated from these decadal values. Yearly values could easily be provided, but specifying the data in terms of decadal averages makes the climatology easier to change. Because the CEDS only includes emissions through 2014, the last decadal value in 2010 is an average over the 10-year period between 2005 and 2014.

Determining the E_i by SO₂ emissions alone is not the same as assuming that only SO₂ contributes to the anthro-

Table 5. Weights of precursor emission components.

k	w_k	Scales with
1	0.645	SO ₂ emissions
2	0.355	NH ₃ emissions

pogenic aerosol, but rather that other anthropogenic aerosol and precursor compound emissions scale with the emission of SO₂, an important but subtle distinction. Scaling anthropogenic aerosol forcing by SO₂ emissions alone appears to reasonably capture the behavior of CMIP5 models (Stevens, 2015). Nonetheless, there is some evidence that aerosol forcing may have begun to decouple from SO₂ emissions with the onset of more stringent air quality controls in some countries beginning in the late 1970s and will increasingly do so in the future (Bellouin et al., 2011). To allow for this possibility, we add a second component which scales like the NH₃ emissions. The relative weight of these two components is chosen so that the optical depth of the plume associated with the NH₃ component is one-third of that from SO₂ in the year 2005 (Table 5). This ratio of one-third was chosen to match the ratio between present-day sulfate and ammonia forcing in the AeroCom II models (Myhre et al., 2013).

As intended, the addition of an NH₃ component to the temporal scaling moderates the effect of air quality regulations since the late 1970s. This is shown in Fig. 9. The blue dashed curve in the upper panel describes the relative contribution of aerosol precursors which scale like SO₂. A value of 0.5, as is, for instance, evident around 1950, means that these precursors contributed to a global anthropogenic AOD relative to 1850 that is 50% of what it was in 2005. The green dashed curve shows the same for components that scale with NH₃ emissions, and together the blue and green curves sum to $E(t_y)$, as shown by the black curve. Absolute values of

Table 6. Equivalent SO₂ emissions for the different plumes in different years in Tg SO₂. The fraction of emissions of black carbon, relative to the fraction in 2005 is shown in parentheses. A value of 0.3 means that the black carbon fraction was 30 % of the 2005 black carbon fraction in a given region.

No.	Source region	1900	1950	1980	2005	2014
1	Europe	8.95 (2.52)	18.26 (1.91)	56.80 (0.84)	16.41 (1.00)	11.35(1.19)
2	North America	7.65 (2.41)	24.09 (1.05)	29.32 (0.81)	17.45 (1.00)	7.39 (1.57)
3	East Asia	0.17 (0.01)	1.69 (0.95)	14.72 (0.98)	37.36 (1.00)	34.89 (1.34)
4	South Asia	0.18 (3.80)	1.57 (1.62)	9.18 (0.98)	17.17 (1.00)	22.89 (0.97)
5	North Africa	0.08 (1.36)	0.20 (1.23)	1.02 (0.94)	1.70 (1.00)	1.94 (0.99)
6	South America	0.12 (2.75)	1.24 (1.12)	4.81 (0.85)	4.88 (1.00)	5.26 (1.09)
7	Maritime Continent	0.03 (3.34)	0.22 (1.93)	2.13 (0.87)	4.15 (1.00)	4.43 (1.07)
8	South central Africa	0.04 (2.71)	1.42 (0.66)	3.83 (0.53)	3.35 (1.00)	4.29 (1.01)
9	Australia	0.23 (1.29)	0.63 (1.18)	1.61 (1.08)	1.57 (1.00)	1.39 (1.14)

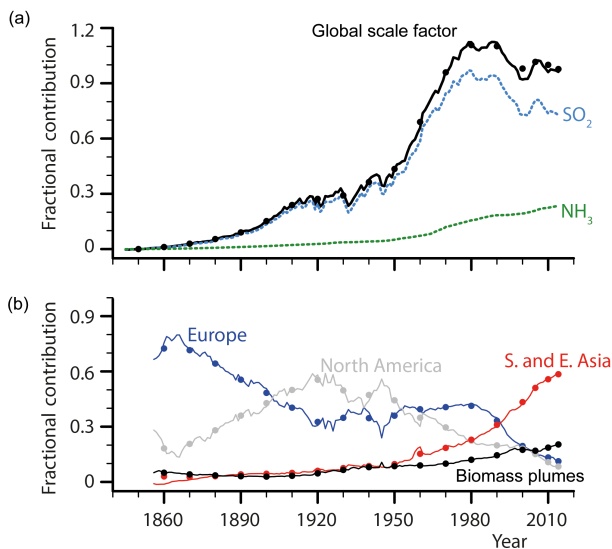


Figure 9. Contributions to anthropogenic AOD distribution. The annual scaling factor for the global emissions, $E(t_y)$ shows the strength of the globally averaged post-1850 anthropogenic AOD relative to its value in 2005, along with the relative weighting of its precursors which scale with SO₂ versus NH₃ emissions, respectively, panel (a). Contributions (panel b) from the $E_i(t_y)$ by different regions to $E(t_y)$. Contributions (panel b) from four regions: Europe (blue), North America (grey), south and east Asia (red) and the four biomass plumes (black). The 11-year averages centered on the middle year of a decadal average are shown by filled circles. The departure between the circles and the lines for the Asian plumes in 1850 is because emissions over east Asia are estimated to have decreased in the first decade after 1850, and the decadal scaling coefficients were not allowed to be negative.

the equivalent SO₂ emissions plus 0.55 times NH₃ emissions (each measured in Tg), and the relative contribution of absorbing aerosol emissions, are tabulated for different time periods for the different plumes in Table 6.

Other factors, which do not correlate with regional NH₃ and SO₂ emissions, may also influence the amplitude of an-

thropogenic aerosol plumes. However, a direct link to emissions is simple, transparent and appears to capture the main features seen in more complex models. This is evident both in terms of the temporal trend in the global signal (Stevens, 2015) and in shifts of regional patterns, e.g., the very large regional shifts in aerosol loading over the last 40 years. Prior to the 1990s, emissions from North America and Europe dominated contributions to the anthropogenic aerosol. Thereafter, Asian sources became more important. This is shown in the lower panel of Fig. 9, where the relative contributions to E from a particular plume, E_i , or a group of plumes, is plotted. It shows, for instance, that according to MACv2-SP, in the year 2010, south and east Asia were responsible for 60 % of the total anthropogenic aerosol. Before 1970 emissions in the Atlantic sector were responsible for the vast majority of emissions. Changes in emissions over Europe rather than North America appear to be more important for the rapid rise of emissions, from about half their present-day values in 1950 to their local maximum around 1980. Because European emissions are more centered over the continent, one would expect this rise to be somewhat less effective than it would have been had it been associated with North American sources. The emissions history also suggests that the overwhelming amount of emissions have and continue to be dominated by Northern Hemisphere sources.

In the present implementation, the single-scattering albedo of the individual plumes does not vary with time. A different balance of emissions of absorbing versus scattering aerosols can be evaluated by comparing estimates of historical black carbon emissions to the emission factors used to scale the amplitudes of the MACv2-SP plumes. This ratio is plotted in Fig. 10 and suggests that the ratio was more or less constant over the first half of the last century, and began to decrease after around 1980 as efforts were made to limit SO₂ emissions. A more absorbing anthropogenic aerosol would, all else being equal, lead to less radiative forcing per unit optical depth. The effects on the regional scale can be large, as is demonstrated by comparing the change in the ratio of black carbon to equivalent SO₂ emissions over the historical

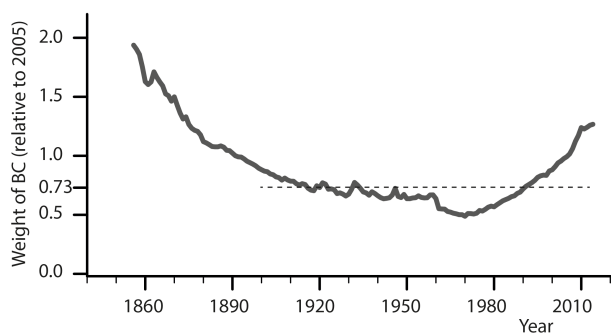


Figure 10. Relative weight of black carbon emissions versus equivalent SO_2 emissions as compared to a value of unity in 2005. For example, a value of 0.75 in 1920 implies that the emissions of black carbon relative to the weighted SO_2 and NH_3 emissions were 75 % of their 2005 value. The dashed line, corresponding to a ratio of 0.73, is the mean from 1900 to the present.

record (e.g., Table 6). Based on the CEDS data, the amount of black carbon emissions per unit equivalent SO_2 emissions was about twice as large over Europe in 1950 as it was in 2005. This apparent brightening of the aerosol prior to about 1970 suggests that aerosol forcing in the period before extensive efforts to reduce SO_2 emissions in the 1970s would have contributed to the radiative efficiency of the aerosol increasing with time, decreasing again after 1980. For the present, such effects are not included in MACv2-SP, which does not consider aerosol composition changes for biomass and industrial plumes over time. In light of the arguments of Stevens (2015), experiments to judge the magnitude of such changes are warranted.

5 Assessing MACv2-SP: climatology and radiative forcing

5.1 Aerosol optical depth and cloud active properties climatology

MACv2-SP appears to do an adequate job in capturing the main features of the MACv2 climatology of the anthropogenic aerosol. This is illustrated in Fig. 11, where we compare 2 months of the MACv2 climatology with MACv2-SP. The main centers of action over North and South America, Asia, central Africa and northern Australia, as well as the more complex structure of the aerosol over south and east Asia, extending over the Maritime Continent appear to be well fit. The seasonal shift between March, where the Asian aerosol is more extended over the Pacific, to September, where Southern Hemisphere and equatorial biomass burning regions are more pronounced, is also well represented by MACv2-SP. As compared to Fig. 2, the treatment of the vertical distribution also helps capture the reduction in column anthropogenic aerosol burden in regions of elevated terrain. This is most evident over the Tibetan Plateau but is also ap-

Table 7. Metrics of optical depth for the total (anthropogenic and natural) aerosol. Shown are the global values, the hemispheric ratio and the root mean square difference. For the AeroCom models, this is calculated with respect to the AeroCom mean; for MACv2-SP, this is calculated relative to MACv2. In the case of the total aerosol, for the AeroCom models, we consider 26 calculations and disregard the outliers by showing the values of the first and third quartiles and the median. For the anthropogenic aerosol, the tabulated results are taken from Table 2 of Myhre et al. (2013).

Aerosol	Global	NH / SH	RMSE	Anthropogenic
MACv2	0.124	1.99	n/a	0.030
MACv2-SP	0.121	1.93	0.019	0.028
AeroCom Q1	0.116	1.52	0.048	0.026
AeroCom median	0.131	1.94	0.063	0.027
AeroCom Q3	0.150	2.19	0.071	0.040

parent over the Altiplano, near Bolivia, and to a lesser extent over the Alps. Compared to MACv2, MACv2-SP has a more compact spatial footprint, with less column burden of anthropogenic aerosol in the Southern Hemisphere, and the structure of the main aerosol plumes is smoother, reflecting the shape of the underlying plumes. This smoothness causes a somewhat greater eastward extent, for instance, of the Asian aerosol. These types of biases may exaggerate the downstream effect of the cloud active aerosol as they will project effectively onto maritime clouds and hence radiative forcing.

To more quantitatively estimate how well MACv2-SP represents understanding of the present-day anthropogenic aerosol distribution, we calculate some global measures and compare them to the spread across state-of-the-art aerosol climate models participating in the AeroCom project. In Table 7, we summarize the global and hemispheric total column AODs in MACv2-SP and the anthropogenic (relative to 1850) contribution. MACv2 is well within the range of the AeroCom models, with an AOD midway between the AeroCom median and second quartile, but a slightly larger anthropogenic component. The hemispheric asymmetry in MACv2 is near, but slightly larger than the AeroCom median, but well within the interquartile spread. The diversity of the AeroCom model spatial distributions, as measured by the root mean square difference from the AeroCom mean, is much larger than the root mean square distance between MACv2 and MACv2-SP. The smallest root mean square distance of any of the AeroCom models is 0.031, more than 50 % greater than the mean distance between MACv2-SP and MACv2. MACv2-SP thus lies well within the space of aerosol distributions described by more comprehensive models, is a good fit to MACv2 and is the basis for our claim that MACv2-SP provides an adequate representation of the anthropogenic aerosol.

The parameterized impact of the anthropogenic aerosol on the droplet population density results in a nearly 10 % in-

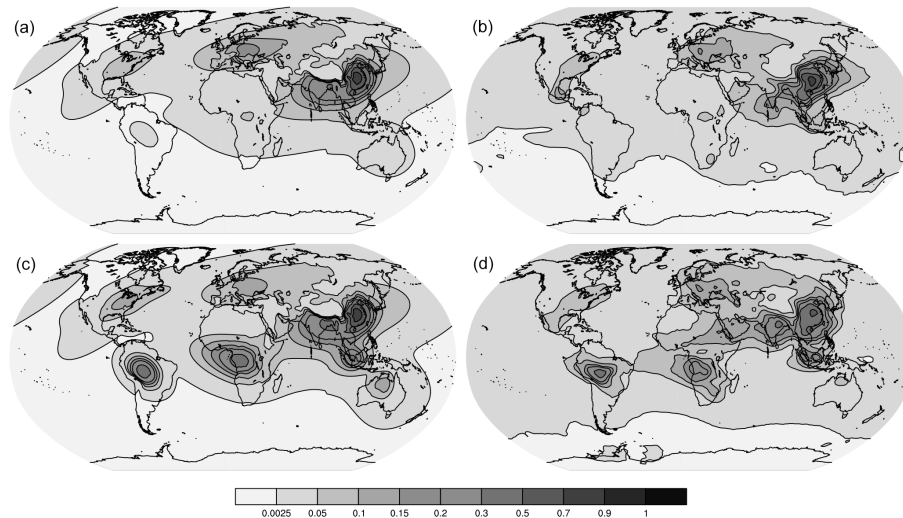


Figure 11. Anthropogenic aerosol optical depth (550 nm), for March and September, from MACv2-SP and MACv2. MACv2-SP (March, panel a; September, panel c), MACv2 (March, panel b; September, panel d). Scale is distorted for low AOD to better illustrate very low values.

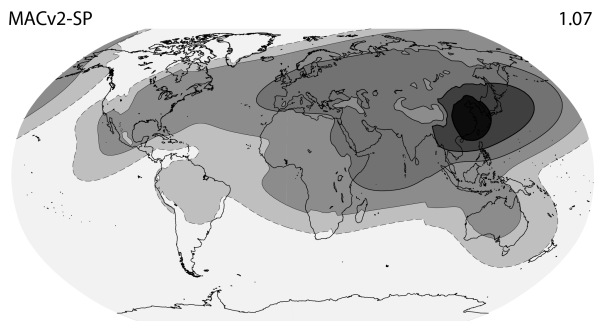


Figure 12. Proportional change between 2005 and 1850 in cloud droplet population density associated with anthropogenic aerosol. Contour levels denote a 2 (dashed), 7, 15, 25 and 35 % (thickened) increase in population density. The global average of the spatial distribution of ratios is given on the upper right.

crease in N . In the vicinity of pollution sources, the effect can be much larger. Figure 12 illustrates the annually averaged effect, which is concentrated over the main industrial plumes. Regionally, this can lead to an annual mean increase in droplet population densities by over 35 %. The global mean change in N , assuming clouds are equally likely everywhere, is a little over 7 %.

Based on ice-core data, Charlson et al. (1992) assumed that droplet population density increases by roughly twice this value, or 15 %. After the massive aerosol infusions associated with the Bárðarbunga eruption of 2014, which led to local AOD perturbations of 0.2, droplet population densities increased by only 50 % (Haywood et al., 2017). Likewise, local droplet perturbations accompanying large aerosol perturbations associated with ship tracks (Christensen and

Stevens, 2011) are found to be of a similar magnitude. The idea that the global influence of aerosol perturbations may not be so large is also supported by the idea of larger background concentrations following the identification of additional natural (biogenic) pathways to new particle formation (e.g., Kirkby et al., 2016). These findings imply a lesser dependence of cloud active aerosol on human-related SO_2 perturbations. Stevens (2015) argued that a global change of 15 % is a reasonable upper bound when one considers evidence from ship tracks. Because MACv2-SP does not interact with the meteorology, a smaller perturbation is required to capture the same radiative effect if the covariance between the aerosol perturbation and cloudiness is negative. Based on these arguments, we believe that the changes in droplet population densities, $\delta N/N$, parameterized by MACv2-SP, provide a reasonable estimate of the radiative effect associated with the anthropogenic aerosol. Nonetheless, given a poor understanding of the relationship between droplet population densities and bulk properties of the ambient aerosol, this number comes with considerable uncertainty. One advantage of MACv2-SP is the ease with which this uncertainty can be sampled, as is explored further in a companion study by Fiedler et al. (2017).

5.2 Structure and estimates of radiative forcing from MACv2-SP

To give an idea of how much forcing is actually associated with MACv2-SP and to test its implementation within an Earth system model, we have made estimates of the radiative forcing associated MACv2-SP using the Max Planck Institute Earth System Model (MPI-ESM1.2; Giorgetta et al., 2013; Stevens et al., 2013) using an updated atmosphere

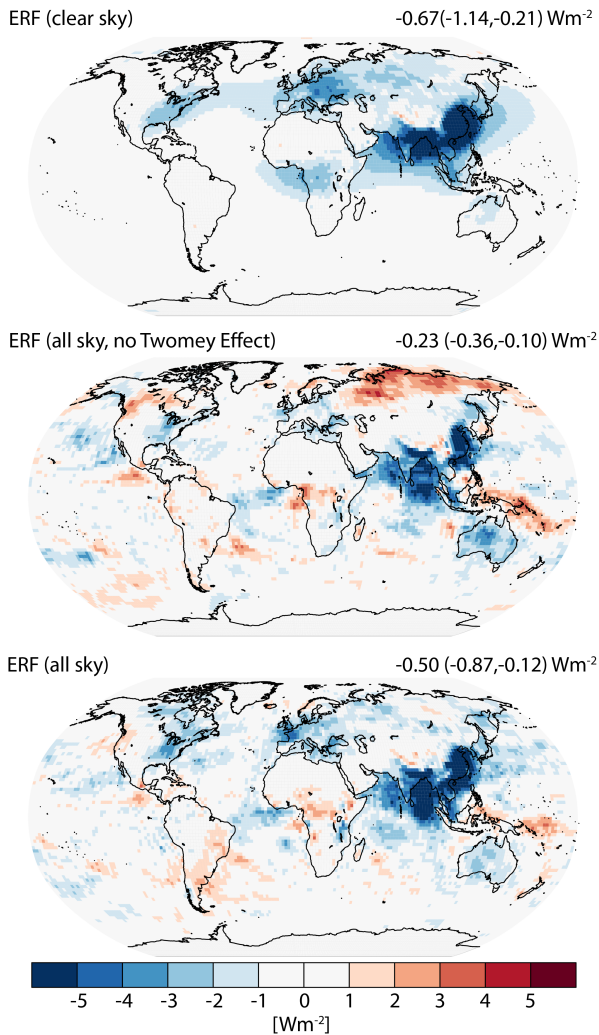


Figure 13. Effective radiative forcing (ERF) and its breakdown into different components: clear-sky ERF (upper panel); all-sky ERF without aerosol–cloud interaction (middle); all-sky ERF with aerosol–cloud interaction (bottom). The numbers on the top right of the figure denote the global mean and the Northern Hemisphere and Southern Hemisphere mean, respectively.

component, ECHAM6.3, which will be used in the new version (1.2) of this model. AMIP (Atmosphere Model Intercomparison Project) type runs were used for this analysis. The radiative forcing has been calculated from a three-member ensemble in two different ways. Instantaneous radiative forcing is estimated from an AMIP run by differencing the results from two calls to the radiation at each radiation time step. In one call, the radiative properties correspond to the given atmospheric state and the pre-industrial (control run) aerosol, and in a second call, the pre-industrial aerosol and assumed cloud-droplet population density are augmented by the anthropogenic perturbation provided by MACv2-SP. The model integrates the radiative heating rates calculated in the second call. A period of 11 years (2000–

2010) is simulated with sea surface temperatures and sea-ice concentrations prescribed. To exclude possible effects of the initial conditions, the first year was excluded from the analysis. Hence, the model samples a variety of atmospheric states over the subsequent 10 years. Each of the 11 simulated years has the same annual cycle of anthropogenic aerosol properties. We also calculate the effective radiative forcing (ERF) by comparing an ensemble of three AMIP simulations for the 2000–2011 period using the 2005 MACv2-SP anthropogenic aerosol added to an 1850 (pre-industrial) background aerosol with an ensemble of five simulations for the same period using just this background aerosol. The difference between the instantaneous and effective radiative forcing gives an estimate of the atmospheric adjustments (Sherwood et al., 2015).

The clear-sky ERF is estimated at -0.67 W m^{-2} , (-0.66 W m^{-2} when calculated using a double radiation call) and its spatial pattern, shown in the upper panel of Fig. 13, is what one expects given the distribution of MACv2-SP AOD, cf. Fig. 11. To estimate how natural variability contributes to uncertainty in the estimate of the ERF, we have compared the standard deviation in reflected shortwave radiation (0.08 W m^{-2}) for an 11-year period across a 100-member ensemble (Stevens, 2015) of our coupled Earth system model. For a three-member ensemble, this level of variability implies a 2σ uncertainty in the ERF estimates of about 0.09 W m^{-2} . This estimate of the uncertainty is consistent with the spread across individual ensemble members and is somewhat less for the clear-sky estimates. Given that the global and annually averaged anthropogenic AOD in MACv2-SP is 0.027, a clear-sky ERF of -0.67 W m^{-2} corresponds to a radiative efficiency of -24 W m^{-2} per unit optical depth. This is in agreement with past modeling. In a comparison of 16 state-of-the-art chemistry climate models, Myhre et al. (2013) calculated a median radiative efficiency of -24 W m^{-2} and, excluding one obvious outlier, the most negative radiative efficiency among the models is -27.4 W m^{-2} .

As a sensitivity study, we performed two additional simulations with different values of ω in industrial plumes. In one simulation, ω , whose base value is 0.93, was increased to 0.96. In a second simulation, it was decreased to 0.87, giving the industrial plumes the same value of ω as the biomass-burning-dominated plumes. Increasing the single-scattering albedo by 0.03 increases the clear-sky ERF to -0.77 W m^{-2} . Likewise, decreasing it by 0.06 reduces the clear-sky ERF to -0.46 W m^{-2} . From this it appears that, for small changes in the ω of the industrial plumes, the clear-sky ERF (and the radiative efficiency) responds roughly linearly in ω_i with $d(\text{ERF})/d\omega_i \approx -3.33 \text{ W m}^{-2}$.

By increasing the background albedo, clouds reduce the clear-sky ERF by about a factor of 3 from what it would be if there were no clouds. This is illustrated by comparing the clear-sky ERF (-0.67 W m^{-2}) to the all-sky ERF in a simulation in which aerosol–cloud interactions are neglected. The middle panel of Fig. 13 presents the result of this calculation.

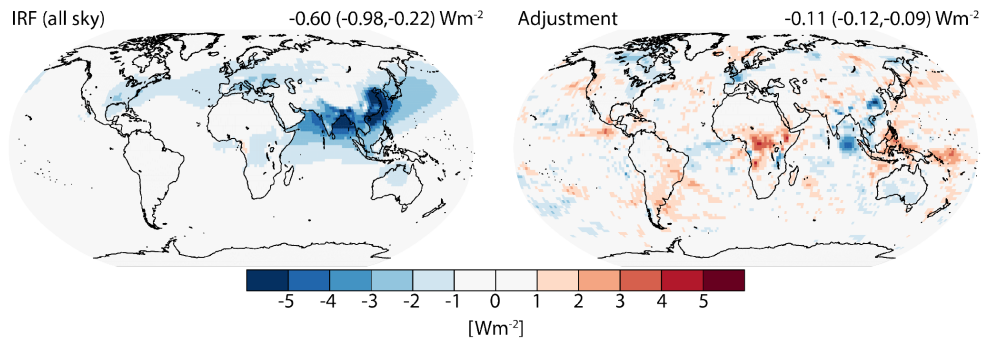


Figure 14. Annual means of instantaneous radiative forcing and adjustments. Instantaneous radiative forcing is shown as calculated using a double radiation call (left) and difference between IRF and ERF, i.e., adjustments (right).

Without aerosol–cloud interactions, the all-sky ERF is about -0.23 W m^{-2} . We call this effect of clouds a “cloud masking” as the clouds mask (or alter) the radiative effect from changes to the clear-sky aerosol, even in cases where the clear-sky aerosol is above the cloud. The simulations yield a cloud masking factor of 0.33. In the AeroCom Phase II models analyzed by Myhre et al. (2013), the median cloud masking factor is 0.37, with considerable scatter among models. The MACv2-SP implementation of the anthropogenic aerosol in the MPI-ESM1.2 gives an all-sky radiative forcing from aerosol–radiation interactions (-8.5 W m^{-2} per unit optical depth), in agreement with the median of the AeroCom II model (-9 W m^{-2}).

Part of the damping of aerosol–radiation interactions by clouds is offset when clouds are allowed to be influenced by the aerosol. Including a Twomey effect parameterized by MACv2-SP increases the magnitude of the ERF to -0.50 W m^{-2} so that overall clouds contribute to a small reduction in the magnitude of the ERF over what one would calculate were there no clouds in the atmosphere. In a companion paper, Fiedler et al. (2017) explore the degree to which aerosol–cloud interactions offset the cloud masking effect on aerosol–radiation interactions and show that this depends primarily on how pristine one assumes the background atmosphere to be.

Differences between the ERF and instantaneous radiative forcing (IRF) suggest that changes in the system, adjustments, act to reduce the forcing by about 20 %. Double radiation calls yield very stable estimates of the IRF in our model, with a pattern more similar to the distribution of the aerosol than that of the clear-sky ERF. This is illustrated in the left panel of Fig. 14. The figure also illustrates that the IRF is more negative than the all-sky ERF. The pattern of adjustments will be sensitive to noise in the regional structure of ERF estimates, despite an attempt to minimize these through the use of a long runs (10 years) and ensembles of simulations, so that we hesitate to overinterpret its structure. It will be interesting to see if other models forced with the same aerosol MACv2-SP produce similar patterns of adjustments.

6 Conclusions

An empirically based analytic parameterization of anthropogenic (post-1850) aerosol optical properties and their associated Twomey effect, MACv2-SP, has been developed for use in climate modeling studies. MACv2-SP is empirical in that it is fit to the gridded MACv2 climatology, and thereby is directly constrained by understanding and measurements of the spatial distribution of the present-day anthropogenic aerosol. An analytic description was motivated by a desire to ease implementation and input data requirements, thereby helping ensure that the climatology could be consistently implemented across a range of models, including very-high-resolution models, and also varied easily. By describing the aerosol in terms of the post-1850 anthropogenic perturbation, MACv2-SP avoids the problem of perturbing the control climate of models in which it is implemented. By proposing a plausible representation of the anthropogenic aerosol that can be consistently implemented in many climate models, robust and consistent responses to aerosol forcing may emerge and these could provide a stronger top-down constraint on the magnitude of that forcing.

It is demonstrated that a plume-based model, which we call MACv2-SP, with relatively few degrees of freedom adequately captures the more complex MACv2 grid-point climatology. A total of nine plumes, describing the patterns of aerosol optical properties attributable to major emission regions, were sufficient to capture spatial variations in the anthropogenic aerosol. Each plume is in turn constructed from two independent features designed to capture differences in the near- and far-field aerosol response to sources and differences in meteorology that shape the plumes. Account was also taken of the annual cycle, the vertical distribution and the spectral dependence of aerosol optical properties. Perturbations to cloud active properties associated with the anthropogenic aerosol were scaled by fine-mode aerosol optical depth, using relationships derived from observational data and more comprehensive modeling. Despite its vastly reduced number of degrees of freedom, MACv2-SP is capa-

ble of reproducing the spatial distribution and amplitude of the anthropogenic AOD in MACv2, fitting the observations better (RMSE of 0.19 versus an AeroCom median RMSE of 0.63) than what is presently possible using process-based models. Other features, such as total AOD and the ratio of Northern Hemisphere to Southern Hemisphere loading, are also well captured by MACv2-SP.

MACv2-SP represents temporal variations in the anthropogenic aerosol by scaling the strength of its plumes in the year 2005 by estimates of historic (or possibly projections of future) emissions. In deriving the temporal scaling, both nitrate-like and sulfate-like aerosol precursors are accounted for. By “nitrate-like” or “sulfate-like” we mean that the temporal scaling of the precursors is like ammonia or like sulfur dioxide, but could in reality be attributable to a broader range of anthropogenic aerosol sources. These scaling factors are derived by associating national emission inventories with the nine plumes and provide a simple way of linking knowledge of aerosol emissions to plausible patterns of radiative forcing.

The approach underlying MACv2-SP is based on a single or guiding assumption: the difference between the climate response by a model using a fully interactive description of the aerosol, as compared to a climatological description of aerosol properties tuned to give the same radiative forcing, is small as compared to uncertainties arising from other sources, e.g., cloud parameterizations. This assumption, though common to any climatology, emphasizes that MACv2-SP is meant to be a reference aerosol-forcing climatology, not a reference aerosol climatology. Serving this purpose requires sufficient degrees of freedom to match both the radiative forcing arising from aerosol–cloud interactions and aerosol–radiation interactions, at the surface and the top of the atmosphere, and also describe the large-scale pattern of regional forcing. As a reference forcing climatology, MACv2-SP should not be interpreted in terms of its nominal physical parameters, but rather in terms of the radiative forcing it produces.

In constructing MACv2-SP, we have made a number of simplifications or secondary assumptions. We call these “secondary” because they are easy to modify without altering the basic approach. Nonetheless, because these simplifications reflect our beliefs as to what features of the anthropogenic aerosol are unimportant to the climate response, they are itemized here in the hope that they might help guide and focus future research. These are

- S1:** that MACv2 adequately describes the spatial distribution of the anthropogenic aerosol;
- S2:** that the anthropogenic aerosol burden associated with a given plume scales linearly with the weighted emissions of anthropogenic SO₂ and NH₃ in the geographic vicinity of that plume;

- S3:** that the annual cycle affects only the amplitude of plume features but not their shape, and that the strength (amplitude) of the seasonal cycle is proportional to the mean strength of each plume feature;

- S4:** that the climate response attributable to changes in the character of the aerosol over time (as measured by its cloud activity, and intensive properties like single-scattering albedo or asymmetry factor), are small as compared to changes in extensive properties, i.e., the anthropogenic aerosol optical depth;

- S5:** that the local effect of the aerosol on cloud optical properties scales logarithmically with a linear function of anthropogenic fine-mode aerosol.

The climatology is constructed in a manner that makes it easy to relax and test many of these assumptions. For instance, the parameterization of the Twomey effect is easy to modify; likewise, the assumption that the single-scattering albedo of industrial plumes have not changed over the historical period can be relaxed. Although focusing on the simplifications itemized above encourages the thought that the climatological approach is too simple, it may well be that it is already more detailed than is really necessary for most purposes. For instance, there is scant evidence that many of the features which we endeavor to incorporate, such as the seasonal cycle, details of the plume shape or even such a large number of plumes, are important for the climate response. For this reason, future work should also explore the effect of simplifying MACv2-SP, as it may well turn out that even a substantially simpler implementation can capture the main response of the climate system to forcing.

MACv2-SP is implemented into the Earth system model of the Max Planck Institute for Meteorology (the MPI-ESM1.2), and an ensemble of simulations is used to estimate instantaneous and effective radiative forcing. Both forcing estimates for clear-sky and all-sky conditions are calculated. The all-sky effective radiative forcing is estimated from the simulations to be -0.5 W m^{-2} . Clouds, by masking aerosol–radiation interactions, diminish the forcing, something that is partially offset by accounting for aerosol–cloud interactions. As a result, the net effect of clouds on aerosol radiative forcing is small but slightly positive, as the clear-sky effective radiative forcing (-0.67 W m^{-2}) is more negative than the all-sky radiative forcing (-0.50 W m^{-2}). Because cloud masking effects are not independent of the aerosol–cloud interactions, the effect of clouds, which are small here, can be inflated if the two effects are considered independently, as is usually the case. An instantaneous radiative forcing (all-sky) of -0.6 W m^{-2} is associated with the MPI-ESM1.2 implementation of MACv2-SP, as estimated from a double call to radiation. Adjustments, defined as the difference between the effective and instantaneous radiative forcing thus also act to weaken the overall forcing by about 20 %.

Though an effort has been made to characterize different measures of the radiative forcing associated with the MPI-ESM1.2 implementation of MACv2-SP, these numbers are intended more as a characterization of MACv2-SP and less as a new estimate of aerosol forcing. Although developed to mimic MACv2 and the synthesis of past AeroCom studies, MACv2 has been formulated so that it should be easy to adjust parameters to match other estimates of forcing, for instance, to allow for more potent aerosol–cloud interactions. The real purpose behind the development of MACv2-SP is to enable its use across a range of models in the hope that robust model responses emerge in a way that identifies additional constraints on the magnitude of the forcing, for instance, through detection and attribution approaches centered around the pattern of the response. Such an effort would be aided if MACv2-SP is adopted for use by other models.

7 Data and code availability

The MACv2-SP climatology, including algorithms and input data used to generate the climatology, is provided as an electronic supplement to this paper. Primary data and scripts used in the analysis and other supplementary information that may be useful in reproducing the author's work are archived by the Max Planck Institute for Meteorology and can be obtained by contacting publications@mpimet.mpg.de.

The Supplement related to this article is available online at [doi:10.5194/gmd-10-433-2017-supplement](https://doi.org/10.5194/gmd-10-433-2017-supplement).

Author contributions. Bjorn Stevens conceived the simple plume model, implemented it based on a prototype developed by the whole team and wrote the paper. Stephanie Fiedler helped with the implementation and tuning of the model and contributed to the writing of the paper. Stephanie Fiedler, Bjorn Stevens and Thorsten Mauritsen designed and evaluated the ECHAM experiments which were performed by Thorsten Mauritsen and Stephanie Fiedler. Stefan Kinne led the development of the underlying MACv2 climatology, performed the offline radiative calculations, advised on the design of the plume model and, together with Jobst Müsse, Bjorn Stevens and Stephanie Fiedler, designed the cloud active component. Jobst Müsse performed the analysis of the AeroCom II models and climatological datasets of droplet number. Steven J. Smith helped with the provision of the historical forcing data. Karsten Peters and Sebastian Rast designed the plume model, contributed text describing its formulation and provided the initial tuning of this model.

Competing interests. The authors declare that they have no conflict of interest.

Acknowledgements. The authors acknowledge the generous and unfettered support of the Max Planck Society. Use of the super-computer facilities at the Deutsches Klimarechenzentrum (DKRZ) is acknowledged as is funding from the FP7 project BACCHUS (no. 603445). Aiko Voigt is thanked for contributions to the early development of the plume ideas. The reviewers are acknowledged for their constructive contributions to the improvement of the presentation of our ideas.

The article processing charges for this open-access publication were covered by the Max Planck Society.

Edited by: J. Williams

Reviewed by: three anonymous referees

References

- Andreae, M. O.: Correlation between cloud condensation nuclei concentration and aerosol optical thickness in remote and polluted regions, *Atmos. Chem. Phys.*, 9, 543–556, doi:10.5194/acp-9-543-2009, 2009.
- Baker, M. B. and Charlson, R. J.: Bistability of CCN concentrations and thermodynamics in the cloud-topped boundary layer, *Nature*, 345, 142–145, 1990.
- Bellouin, N., Rae, J., Jones, A., Johnson, C., Haywood, J., and Boucher, O.: Aerosol forcing in the Climate Model Intercomparison Project (CMIP5) simulations by HadGEM2-ES and the role of ammonium nitrate, *J. Geophys. Res.-Atmos.*, 116, D20206, doi:10.1029/2011JD016074, 2011.
- Bennartz, R.: Global assessment of marine boundary layer cloud droplet number concentration from satellite, *J. Geophys. Res.-Atmos.*, 112, D02201, doi:10.1029/2006JD007547, 2007.
- Bollasina, M. A., Ming, Y., and Ramaswamy, V.: Anthropogenic Aerosols and the Weakening of the South Asian Summer Monsoon, *Science*, 334, 502–505, 2011.
- Boucher, O. and Lohmann, U.: The sulfate-CCN-cloud albedo effect: A sensitivity study with two general circulation models, *Tellus B*, 47, 281–300, 1995.
- Boucher, O., Randall, D., Artaxo, P., Bretherton, C., Feingold, G., Forster, P., Kerminen, V.-M., Kondo, Y., Liao, H., Lohmann, U., Rasch, P., Satheesh, S. K., Sherwood, S., Stevens, B., and Zhang, X. Y.: Clouds and Aerosols, in: *Climate Change 2013: The Physical Science Basis, Contribution of Working Group I to the Fifth Assessment Report of the Intergovernmental Panel on Climate Change*, edited by: Stocker, T. F., Qin, D., Plattner, G. K., Tignor, M., Allen, S. K., Boschung, J., Nauels, A., Xia, Y., Bex, V., and Midgley, P. M., Cambridge University Press, Cambridge, UK, New York, NY, USA, 571–657, 2013.
- Brenguier, J. L., Pawlowska, H., and Schüller, L.: Radiative properties of boundary layer clouds: Droplet effective radius versus number concentration, *J. Atmos. Sci.*, 57, 803–821, 2000.
- Carlsaw, K. S., Lee, L. A., Reddington, C. L., Pringle, K. J., Rap, A., Forster, P. M., Mann, G. W., Spracklen, D. V., Woodhouse, M. T., Regayre, L. A., and Pierce, J. R.: Large contribution of natural aerosols to uncertainty in indirect forcing, *Nature*, 503, 67–71, 2013.

- Charlson, R. J., Schwartz, S. E., Hales, J. M., Cess, R. D., Coakley, J. A., Hansen, J. E., and Hofmann, D. J.: Climate Forcing by Anthropogenic Aerosols, *Science*, 255, 423–430, 1992.
- Christensen, M. W. and Stephens, G. L.: Microphysical and macrophysical responses of marine stratocumulus polluted by underlying ships: Evidence of cloud deepening, *J. Geophys. Res.-Atmos.*, 116, D03201, doi:10.1029/2010JD014638, 2011.
- Deser, C., Phillips, A. S., Alexander, M. A., and Smoliak, B. V.: Projecting North American Climate over the Next 50 Years: Uncertainty due to Internal Variability, *J. Climate*, 27, 2271–2296, 2014.
- Dubovik, O., Holben, B., Eck, T. F., Smirnov, A., Kaufman, Y. J., King, M. D., Tanré, D., and Slutsker, I.: Variability of Absorption and Optical Properties of Key Aerosol Types Observed in Worldwide Locations, *J. Atmos. Sci.*, 59, 590–608, 2002.
- Eyring, V., Bony, S., Meehl, G. A., Senior, C. A., Stevens, B., Stouffer, R. J., and Taylor, K. E.: Overview of the Coupled Model Intercomparison Project Phase 6 (CMIP6) experimental design and organization, *Geosci. Model Dev.*, 9, 1937–1958, doi:10.5194/gmd-9-1937-2016, 2016.
- Fiedler, S., Stevens, B., and Mauritsen, T.: On the importance of climate variability and a Twomey effect for the aerosol effective radiative forcing, *J. Adv. Model. Earth Syst.*, in review, 2017.
- Giorgetta, M. A., Jungclaus, J., Reick, C. H., Legutke, S., Bader, J., Böttinger, M., Brovkin, V., Crueger, T., Esch, M., Fieg, K., Glushak, K., Gayler, V., Haak, H., Hollweg, H. D., Ilyina, T., Kinne, S., Kornblueh, L., Matei, D., Mauritsen, T., Mikolajewicz, U., Mueller, W., Notz, D., Pithan, F., Raddatz, T., Rast, S., Redler, R., Roeckner, E., Schmidt, H., Schnur, R., Segschneider, J., Six, K. D., Stockhause, M., Timmreck, C., Wegner, J., Widmann, H., Wieners, K. H., Claussen, M., Marotzke, J., and Stevens, B.: Climate and carbon cycle changes from 1850 to 2100 in MPI-ESM simulations for the Coupled Model Intercomparison Project phase 5, *J. Adv. Model. Earth Syst.*, 5, 572–597, 2013.
- Grosvenor, D. P. and Wood, R.: The effect of solar zenith angle on MODIS cloud optical and microphysical retrievals within marine liquid water clouds, *Atmos. Chem. Phys.*, 14, 7291–7321, doi:10.5194/acp-14-7291-2014, 2014.
- Haywood, J., Jones, A., Malavelle, F., Gettelman, A., Allan, R. P., Bellouin, N., Boucher, O., Bauduin, S., Carslaw, K. S., Carslaw, K., Clarisse, L., Coe, H., Dalvi, M., Dhomse, S., Grosvenor, D., Hartley, M., Johnson, B., Johnson, C., Knight, J., Kristiansen, J.-E., Mann, G., Myhre, G., O'Connor, F., Platnick, S., Schmidt, A., Stephens, G. L., Stier, P., and Takahashi, H.: Validating global model predictions of aerosol-cloud interactions using a large volcanic fissure eruption, *Nature*, submitted, 2017.
- Holben, B. N., Tanré, D., Smirnov, A., Eck, T. F., Slutsker, I., Abuhassan, N., Newcomb, W., Schafer, J., Catenet, B., Lavenue, F., Kaufman, Y., Vande Castle, J., Setzer, A., Markham, B., Clark, D., Frouin, R., Halthore, R., Karneli, A., O'Neill, N., Pietras, C., Pinker, R., Voss, K., and Zibordi, G.: An emerging ground-based aerosol climatology: Aerosol optical depth from AERONET, *J. Geophys. Res.-Atmos.*, 106, 12067–12097, 2001.
- Khain, A., Lynn, B., and Dudhia, J.: Aerosol Effects on Intensity of Landfalling Hurricanes as Seen from Simulations with the WRF Model with Spectral Bin Microphysics, *J. Atmos. Sci.*, 67, 365–384, 2010.
- Kinne, S., Schulz, M., Textor, C., Guibert, S., Balkanski, Y., Bauer, S. E., Bernsten, T., Berglen, T. F., Boucher, O., Chin, M., Collins, W., Dentener, F., Diehl, T., Easter, R., Feichter, J., Fillmore, D., Ghan, S., Ginoux, P., Gong, S., Grini, A., Hendricks, J., Herzog, M., Horowitz, L., Isaksen, I., Iversen, T., Kirkevåg, A., Kloster, S., Koch, D., Kristjansson, J. E., Krol, M., Lauer, A., Lamarque, J. F., Lesins, G., Liu, X., Lohmann, U., Montanaro, V., Myhre, G., Penner, J., Pitari, G., Reddy, S., Seland, O., Stier, P., Takemura, T., and Tie, X.: An AeroCom initial assessment – optical properties in aerosol component modules of global models, *Atmos. Chem. Phys.*, 6, 1815–1834, doi:10.5194/acp-6-1815-2006, 2006.
- Kinne, S., O'Donnell, D., Stier, P., Kloster, S., Zhang, K., Schmidt, H., Rast, S., Giorgetta, M., Eck, T. F., and Stevens, B.: MAC-v1: A new global aerosol climatology for climate studies, *J. Adv. Model. Earth Syst.*, 5, 704–740, 2013.
- Kirkby, J., Duplissy, J., Sengupta, K., Frege, C., Gordon, H., Williamson, C., Heinritzi, M., Simon, M., Yan, C., Almeida, J., Tröstl, J., Nieminen, T., Ortega, I. K., Wagner, R., Adamov, A., Amorim, A., Bernhammer, A.-K., Bianchi, F., Breitenlechner, M., Brilke, S., Chen, X., Craven, J., Dias, A., Ehrhart, S., Flagan, R. C., Franchin, A., Fuchs, C., Guida, R., Hakala, J., Hoyle, C. R., Jokinen, T., Junninen, H., Kangasluoma, J., Kim, J., Krapf, M., Kürten, A., Laaksonen, A., Lehtipalo, K., Makhmutov, V., Mathot, S., Molteni, U., Onnela, A., Peräkylä, O., Piel, F., Petäjä, T., Praplan, A. P., Pringle, K., Rap, A., Richards, N. A. D., Riipinen, I., Rissanen, M. P., Rondo, L., Sarnela, N., Schobesberger, S., Scott, C. E., Seinfeld, J. H., Sipilä, M., Steiner, G., Stozhkov, Y., Stratmann, F., Tomé, A., Virtanen, A., Vogel, A. L., Wagner, A. C., Wagner, P. E., Weingartner, E., Wimmer, D., Winkler, P. M., Ye, P., Zhang, X., Hansel, A., Dommen, J., Donahue, N. M., Worsnop, D. R., Baltensperger, U., Kulmala, M., Carslaw, K. S., and Curtius, J.: Ion-induced nucleation of pure biogenic particles, *Nature*, 533, 521–526, 2016.
- Leibensperger, E. M., Mickley, L. J., Jacob, D. J., Chen, W.-T., Seinfeld, J. H., Nenes, A., Adams, P. J., Streets, D. G., Kumar, N., and Rind, D.: Climatic effects of 1950–2050 changes in US anthropogenic aerosols – Part 2: Climate response, *Atmos. Chem. Phys.*, 12, 3349–3362, doi:10.5194/acp-12-3349-2012, 2012.
- Meehl, G. A., Hu, A., and Santer, B. D.: The Mid-1970s Climate Shift in the Pacific and the Relative Roles of Forced versus Inherent Decadal Variability, *J. Climate*, 22, 780–792, 2009.
- Murphy, D. M., Solomon, S., Portmann, R. W., Rosenlof, K. H., Forster, P. M., and Wong, T.: An observationally based energy balance for the Earth since 1950, *J. Geophys. Res.-Atmos.*, 114, D17107, doi:10.1029/2009JD012105, 2009.
- Myhre, G., Samset, B. H., Schulz, M., Balkanski, Y., Bauer, S., Bernsten, T. K., Bian, H., Bellouin, N., Chin, M., Diehl, T., Easter, R. C., Feichter, J., Ghan, S. J., Hauglustaine, D., Iversen, T., Kinne, S., Kirkevåg, A., Lamarque, J.-F., Lin, G., Liu, X., Lund, M. T., Luo, G., Ma, X., van Noije, T., Penner, J. E., Rasch, P. J., Ruiz, A., Seland, Ø., Skeie, R. B., Stier, P., Takemura, T., Tsigaridis, K., Wang, P., Wang, Z., Xu, L., Yu, H., Yu, F., Yoon, J.-H., Zhang, K., Zhang, H., and Zhou, C.: Radiative forcing of the direct aerosol effect from AeroCom Phase II simulations, *Atmos. Chem. Phys.*, 13, 1853–1877, doi:10.5194/acp-13-1853-2013, 2013.

- Nakajima, T., King, M. D., Spinhirne, J. D., and Radke, L. F.: Determination of the Optical Thickness and Effective Particle Radius of Clouds from Reflected Solar Radiation Measurements – Part 2: Marine Stratocumulus Observations, *J. Atmos. Sci.*, 48, 728–751, 1991.
- Pincus, R., Forster, P. M., and Stevens, B.: The Radiative Forcing Model Intercomparison Project (RFMIP): experimental protocol for CMIP6, *Geosci. Model Dev.*, 9, 3447–3460, doi:10.5194/gmd-9-3447-2016, 2016.
- Quaas, J., Ming, Y., Menon, S., Takemura, T., Wang, M., Penner, J. E., Gettelman, A., Lohmann, U., Bellouin, N., Boucher, O., Sayer, A. M., Thomas, G. E., McComiskey, A., Feingold, G., Hoose, C., Kristjánsson, J. E., Liu, X., Balkanski, Y., Donner, L. J., Ginoux, P. A., Stier, P., Grandey, B., Feichter, J., Sednev, I., Bauer, S. E., Koch, D., Grainger, R. G., Kirkevåg, A., Iversen, T., Seland, Ø., Easter, R., Ghan, S. J., Rasch, P. J., Morrison, H., Lamarque, J.-F., Iacono, M. J., Kinne, S., and Schulz, M.: Aerosol indirect effects – general circulation model intercomparison and evaluation with satellite data, *Atmos. Chem. Phys.*, 9, 8697–8717, doi:10.5194/acp-9-8697-2009, 2009.
- Ramanathan, V., Crutzen, P. J., Kiehl, J. T., and Rosenfeld, D.: Aerosols, Climate, and the Hydrological Cycle, *Science*, 294, 2119–2124, 2001.
- Schulz, M., Textor, C., Kinne, S., Balkanski, Y., Bauer, S., Berntsen, T., Berglen, T., Boucher, O., Dentener, F., Guibert, S., Isaksen, I. S. A., Iversen, T., Koch, D., Kirkevåg, A., Liu, X., Montanaro, V., Myhre, G., Penner, J. E., Pitari, G., Reddy, S., Seland, Ø., Stier, P., and Takemura, T.: Radiative forcing by aerosols as derived from the AeroCom present-day and pre-industrial simulations, *Atmos. Chem. Phys.*, 6, 5225–5246, doi:10.5194/acp-6-5225-2006, 2006.
- Sherwood, S. C., Bony, S., Boucher, O., Bretherton, C., Forster, P. M., Gregory, J. M., and Stevens, B.: Adjustments in the Forcing-Feedback Framework for Understanding Climate Change, *B. Am. Meteorol. Soc.*, 96, 217–228, 2015.
- Shindell, D. T., Lamarque, J.-F., Schulz, M., Flanner, M., Jiao, C., Chin, M., Young, P. J., Lee, Y. H., Rotstayn, L., Mahowald, N., Milly, G., Faluvegi, G., Balkanski, Y., Collins, W. J., Conley, A. J., Dalsoren, S., Easter, R., Ghan, S., Horowitz, L., Liu, X., Myhre, G., Nagashima, T., Naik, V., Rumbold, S. T., Skeie, R., Sudo, K., Szopa, S., Takemura, T., Voulgarakis, A., Yoon, J.-H., and Lo, F.: Radiative forcing in the ACCMIP historical and future climate simulations, *Atmos. Chem. Phys.*, 13, 2939–2974, doi:10.5194/acp-13-2939-2013, 2013.
- Smirnov, A., Holben, B. N., Slutsker, I., Giles, D. M., McClain, C. R., Eck, T. F., Sakerin, S. M., Macke, A., Croot, P., Zibordi, G., Quinn, P. K., Sciare, J., Kinne, S., Harvey, M., Smyth, T. J., Piketh, S., Zielinski, T., Proshutinsky, A., Goes, J. I., Nelson, N. B., Larouche, P., Radionov, V. F., Goloub, P., Krishna Moorthy, K., Matarrese, R., Robertson, E. J., and Jourdin, F.: Maritime Aerosol Network as a component of Aerosol Robotic Network, *J. Geophys. Res.-Atmos.*, 114, D06204, doi:10.1029/2008JD011257, 2009.
- Stevens, B.: Rethinking the Lower Bound on Aerosol Radiative Forcing, *J. Climate*, 28, 4794–4819, 2015.
- Stevens, B. and Feingold, G.: Untangling aerosol effects on clouds and precipitation in a buffered system, *Nature*, 461, 607–613, 2009.
- Stevens, B., Giorgetta, M., Esch, M., Mauritsen, T., Crueger, T., Rast, S., Salzmann, M., Schmidt, H., Bader, J., Block, K., Brokopf, R., Fast, I., Kinne, S., Kornblüeh, L., Lohmann, U., Pincus, R., Reichler, T., and Roeckner, E.: Atmospheric component of the MPI-M Earth System Model: ECHAM6, *J. Adv. Model. Earth Syst.*, 5, 146–172, 2013.
- Tanré, D., Geleyn, J. F., and Slingo, J. M.: First results of the introduction of an advanced aerosol-radiation interaction in the ECMWF low resolution global model, in: *Aerosols and Their Climatic Effects Proceedings of the Meetings of Experts*, edited by: Gerber, H. and Deepak, A., Hampton, VA, 133–177, 1984.
- Thomas, G. E., Poulsen, C. A., Siddans, R., Carbon, E., Sayer, A. M., and Grainger, R. G.: ORAC v3 Dual-view aerosol retrieval from AATSR, Tech. rep., Oxford University, Oxford, 2011.
- Twomey, S.: The nuclei of natural cloud formation part II: The supersaturation in natural clouds and the variation of cloud droplet concentration, *Pure Appl. Geophys.*, 43, 243–249, 1959.
- Voigt, A., Bony, S., Dufresne, J.-L., and Stevens, B.: The radiative impact of clouds on the shift of the Intertropical Convergence Zone, *Geophys. Res. Lett.*, 41, 4308–4315, 2014.
- Wild, M.: Enlightening Global Dimming and Brightening, *B. Am. Meteorol. Soc.*, 93, 27–37, 2012.
- Zhang, R., Delworth, T. L., Sutton, R., Hodson, D. L. R., Dixon, K. W., Held, I. M., Kushnir, Y., Marshall, J., Ming, Y., Msadek, R., Robson, J., Rosati, A. J., Ting, M., and Vecchi, G. A.: Have Aerosols Caused the Observed Atlantic Multidecadal Variability?, *J. Atmos. Sci.*, 70, 1135–1144, 2013.